

Equilibrium structures of anisometric, quadrupolar particles confined to a monolayer

Thomas Heinemann, Moritz Antlanger, Martial Mazars, Sabine H. L. Klapp, and Gerhard Kahl

Citation: *The Journal of Chemical Physics* **144**, 074504 (2016); doi: 10.1063/1.4941585

View online: <https://doi.org/10.1063/1.4941585>

View Table of Contents: <http://aip.scitation.org/toc/jcp/144/7>

Published by the [American Institute of Physics](#)

Articles you may be interested in

[Coarse-graining strategy for molecular pair interactions: A reaction coordinate study for two- and three-dimensional systems](#)

The Journal of Chemical Physics **146**, 164107 (2017); 10.1063/1.4981207

[Angle-resolved effective potentials for disk-shaped molecules](#)

The Journal of Chemical Physics **141**, 214110 (2014); 10.1063/1.4902824

[Coarse-grained electrostatic interactions of coronene: Towards the crystalline phase](#)

The Journal of Chemical Physics **143**, 174110 (2015); 10.1063/1.4935063

[Effect of the surface charge distribution on the fluid phase behavior of charged colloids and proteins](#)

The Journal of Chemical Physics **145**, 155102 (2016); 10.1063/1.4964613

[Phase behavior of patchy spheroidal fluids](#)

The Journal of Chemical Physics **145**, 214904 (2016); 10.1063/1.4969074

[Coulomb fission in multiply charged molecular clusters: Experiment and theory](#)

The Journal of Chemical Physics **146**, 164302 (2017); 10.1063/1.4981918

PHYSICS TODAY

WHITEPAPERS

ADVANCED LIGHT CURE ADHESIVES

Take a closer look at what these environmentally friendly adhesive systems can do

READ NOW

PRESENTED BY
 MASTERBOND
ADHESIVES | SEALANTS | COATINGS

Equilibrium structures of anisometric, quadrupolar particles confined to a monolayer

Thomas Heinemann,^{1,a),b)} Moritz Antlanger,^{2,a),c)} Martial Mazars,^{3,d)} Sabine H. L. Klapp,^{1,e)} and Gerhard Kahl^{4,f)}

¹*Institut für Theoretische Physik, Technische Universität Berlin, Hardenbergstraße 36, D-10623 Berlin, Germany*

²*Institut für Theoretische Physik, TU Wien, Wiedner Hauptstraße 8-10, A-1040 Wien, Austria*

³*Laboratoire de Physique Théorique (UMR 8627), CNRS, Univ. Paris-Sud, Université Paris-Saclay, 91405 Orsay, France*

⁴*Institut für Theoretische Physik and Center for Computational Materials Science (CMS), TU Wien, Wiedner Hauptstraße 8-10, A-1040 Wien, Austria*

(Received 8 December 2015; accepted 27 January 2016; published online 19 February 2016)

We investigate the structural properties of a two-dimensional system of ellipsoidal particles carrying a linear quadrupole moment in their center. These particles represent a simple model for a variety of uncharged, non-polar conjugated organic molecules. Using optimization tools based on ideas of evolutionary algorithms, we first examine the ground state structures as we vary the aspect ratio of the particles and the pressure. Interestingly, we find, besides the intuitively expected T-like configurations, a variety of complex structures, characterized with up to three different particle orientations. In an effort to explore the impact of thermal fluctuations, we perform constant-pressure molecular dynamics simulations within a range of rather low temperatures. We observe that ground state structures formed by particles with a large aspect ratio are in particular suited to withstand fluctuations up to rather high temperatures. Our comprehensive investigations allow for a deeper understanding of molecular or colloidal monolayer arrangements under the influence of a typical electrostatic interaction on a coarse-grained level. © 2016 AIP Publishing LLC. [<http://dx.doi.org/10.1063/1.4941585>]

I. INTRODUCTION

In recent years there is increasing interest in understanding the film morphologies of anisotropic, conjugated organic molecules at inorganic surfaces. A prime example is systems of optically active molecules at inorganic surfaces; these so-called hybrid inorganic/organic systems (HIOSs) represent a very promising material class in optoelectronics.¹⁻⁴ Typically, the corresponding organic molecules are strongly anisotropic in shape and are characterized by complex charge distributions, often dominated by a quadrupole moment.⁵ By manipulating the orientational structure of such organic layers, it is possible to tune the efficiency of the charge carrier transport⁶ and thus to optimize the efficiency of the hybrid system. Somewhat earlier, organic molecules at interfaces have attracted attention in the context of so-called Langmuir monolayers, that is, two-dimensional (2D) films of typically amphiphilic molecules constrained to a liquid-gas interface.^{7,8} Again, the orientational and translational structure in such systems can be quite complex.

From the theoretical side, a full microscopic treatment of an organic molecular layer is still challenging, and this holds particularly for HIOS (where the substrate is typically

patterned). On the level of atomistic molecular dynamics (MD) simulations, one has to consider a large number of interactions such as atomic bonding, van der Waals (Lennard-Jones) potentials, contributions due to bending or torsion of a molecule (see, e.g., Ref. 9), and electrostatic interactions. Even then, it often turns out that atomistic MD calculations do not correctly predict the arrangement of several particles, one main reason being the insufficient treatment of polarizability effects.¹⁰ An example that demonstrates this issue is the quadrupolar molecule benzene, where a representation via atomic point charges¹¹ or multipoles¹² fails to reproduce the corresponding dimer configuration. This suggests to employ quantum chemical approaches to evaluate the electronic structure of the entire system, instead. However, at the moment, this level of complexity is computationally far too demanding, especially at finite temperatures.

Given these difficulties, the goal of the present paper is to understand *generic* aspects of the structural behavior of quadrupolar, anisotropic molecules at interfaces based on a *coarse-grained* model. Specifically, we investigate a 2D many-particle system composed of ellipse-shaped particles with an embedded, axially symmetric quadrupole tensor (higher-order multipoles are neglected). The quadrupole is oriented along one of the ellipsoidal axes as it is the case, e.g., in benzene¹³ or naphthalene, whose quadrupole tensor nearly has axial symmetry.¹⁴ We further assume that the center of the particles is confined to a 2D plane and that the molecules are allowed to rotate only within this plane.

^{a)}T. Heinemann and M. Antlanger contributed equally to this work.

^{b)}Electronic mail: thomasheinemann@mailbox.tu-berlin.de

^{c)}Electronic mail: moritz.antlanger@tuwien.ac.at

^{d)}Electronic mail: martial.mazars@th.u-psud.fr

^{e)}Electronic mail: klapp@physik.tu-berlin.de

^{f)}Electronic mail: gerhard.kahl@tuwien.ac.at

Interestingly, 2D quadrupolar systems are, so far, rather unexplored. This contrasts the situation in the 3D case, where a considerable amount of pioneering work involving quadrupolar particles at finite temperatures^{15–19} and in the ground state²⁰ is available. On the other hand, there are a number of simulation studies dealing with non-quadrupolar, shape-anisotropic particles in 2D, examples being hard ellipsoids,^{21–24} rectangles²⁵ or hard spherocylinders.²⁶ In particular, the density-driven nematic-isotropic transition of hard ellipsoids was already investigated in Ref. 24 and turned out being continuous or of first order depending on the aspect ratio. We also mention a density functional study²⁷ of 2D systems of anisotropic particles exhibiting isotropic phases and phases with simultaneous orientational and translational order. Thus, the important open question to be explored in the present article concerns the interplay of shape anisotropy and quadrupolar intermolecular interactions.

To this end, we employ two types of numerical calculations, that is, optimization techniques based on ideas of evolutionary algorithms (EA) and constant-pressure MD simulations, revealing the system's behavior in the ground state and at finite temperatures. To facilitate the calculations, the non-electrostatic part of the interaction between two molecules is modeled via a purely repulsive, relatively stiff (but not infinitely hard) pair potential that foots on the ellipse-like contact distance suggested by Berne and Pechukas.²⁸ The analytical form of this pair potential resembles an anisotropic soft-sphere potential but has a higher exponent.²⁹ This potential turned out to be suitable for both type of numerical calculations. Van der Waals interactions between the molecules are entirely neglected. Although this may seem somewhat unrealistic for real molecules, there are several advantages of the resulting (repulsive) potential: it reduces the number of parameters, it allows (as we will demonstrate) for a transferability between results at different system parameters,

and it makes it possible to establish a connection of the present study to investigations of anisotropic colloidal particles in confined geometry.^{30–32}

The remainder of this article is organized as follows. In Sec. II, we introduce the model and the pair interactions in detail. Section III is devoted to the methods used to calculate equilibrium structures (at $T = 0$ and $T > 0$) and corresponding data analysis methods. The resulting ground state structures at different pressures and aspect ratios are presented in Sec. IV A, and the corresponding finite-temperature results are discussed in Sec. IV B. Finally, we summarize our findings in Sec. V. Appendices A–C provide additional, complementary information.

II. MODEL

In our investigations, we consider a two-dimensional system, embedded in the (x, y) -plane, where the anisotropic particles are only allowed to rotate around the z -axis. We use reduced units throughout, introducing parameters σ_0 for the length scale, ϵ_0 for the energy scale, and m_0 for the unit of mass.

Our particles are assumed to have an elliptic shape, characterized by the lengths of the two main axes, σ_{\parallel} and σ_{\perp} ; the indices refer to the orientation of the corresponding axes relative to the linear quadrupolar moment to be introduced below (see Figure 1). Defining a dimensionless shape anisotropy parameter, κ , we impose via

$$\sigma_{\parallel} = \sigma_0 \sqrt{\kappa} \quad \text{and} \quad \sigma_{\perp} = \frac{\sigma_0}{\sqrt{\kappa}}$$

that the surface area of our particles is independent of the actual value of κ . The isometric case of a disc is recovered for $\kappa = 1$.

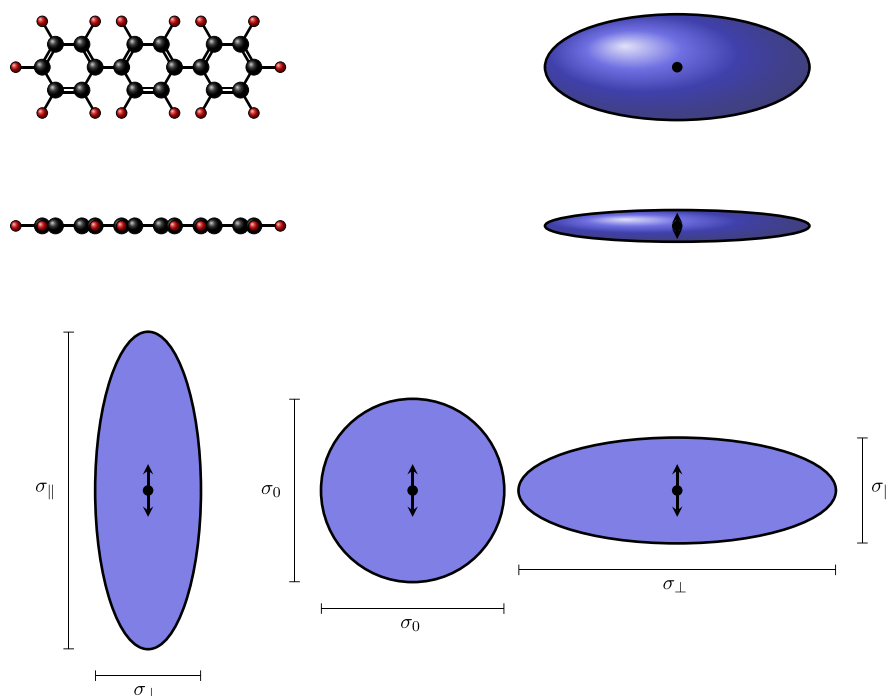


FIG. 1. Taken from Ref. 33. Top-left panel: top and side views of a simple organic molecule shown here is para-terphenyl ($C_{18}H_{14}$), which is composed of three benzene rings. Molecules of this type show a strong anisotropy and feature a complicated charge distribution. Top-right panel: simple organic molecules (as shown in the top-left panel) are modeled in this contribution as soft ellipsoids with an embedded quadrupole moment. Due to the high degree of symmetry of the underlying model, the quadrupole moment is assumed to be linear. Bottom panels: schematic view of our soft, anisometric particles carrying a linear quadrupole moment (visualized by the double-arrow) with $\kappa > 1$ (left panel), $\kappa = 1$ (center panel), and $\kappa < 1$ (right panel). σ_0 , σ_{\parallel} , and σ_{\perp} are defined in the text.

The interaction between two-particles (with indices i and j) can be split into a short-ranged, anisotropic repulsion, $V_{\text{sr}}(\mathbf{r}_{ij}, \hat{\mathbf{u}}_i, \hat{\mathbf{u}}_j)$, and a long-ranged potential, $V_{\text{lr}}(\mathbf{r}_{ij}, \hat{\mathbf{u}}_i, \hat{\mathbf{u}}_j)$; the latter one stems from the interaction of the linear quadrupoles that the particles carry. We define the distance $r_{ij} = |\mathbf{r}_i - \mathbf{r}_j|$ between the centers of the particles and further $\hat{\mathbf{r}}_{ij} = \mathbf{r}_{ij}/r_{ij}$. The $\hat{\mathbf{u}}_i$ and $\hat{\mathbf{u}}_j$ are the normalized orientation vectors of the respective linear quadrupolar moments. Within our model, the shape of the particle is the same for κ and $1/\kappa$, while the respective orientations of the embedded quadrupole moment are perpendicular for the cases κ and $1/\kappa$ (see bottom panels of Figure 1). Consequently, by choosing values of κ both smaller and larger than unity, we are able to consider these two orientations of the quadrupolar moment within the same model.

With the above vectors at hand we introduce

$$a = \hat{\mathbf{u}}_i \cdot \hat{\mathbf{r}}_{ij} \quad b = \hat{\mathbf{u}}_j \cdot \hat{\mathbf{r}}_{ij} \quad c = \hat{\mathbf{u}}_i \cdot \hat{\mathbf{u}}_j. \quad (1)$$

For the short-range contribution of the inter-particle interaction (subscript ‘‘sr’’), we use an anisotropic, repulsive potential: it has the simple functional form of an inverse power law (IPL) interaction, while its dependence on the connecting vector, \mathbf{r}_{ij} , and on the orientations of the quadrupolar moments, $\hat{\mathbf{u}}_i$ and $\hat{\mathbf{u}}_j$, is inspired by a Gay-Berne potential,³⁴

$$V_{\text{sr}}(\mathbf{r}_{ij}, \hat{\mathbf{u}}_i, \hat{\mathbf{u}}_j) = 4\epsilon(\mathbf{r}_{ij}, \hat{\mathbf{u}}_i, \hat{\mathbf{u}}_j) \left[\frac{\sigma(\mathbf{r}_{ij}, \hat{\mathbf{u}}_i, \hat{\mathbf{u}}_j)}{r_{ij}} \right]^{18}, \quad (2)$$

here

$$\epsilon(\mathbf{r}_{ij}, \hat{\mathbf{u}}_i, \hat{\mathbf{u}}_j) = \epsilon_0 = \text{const.}, \quad (3)$$

$$\sigma(\mathbf{r}_{ij}, \hat{\mathbf{u}}_i, \hat{\mathbf{u}}_j) = \sigma_{\perp} \left\{ 1 - \frac{\chi}{2} \left[\frac{(a+b)^2}{1+\chi c} + \frac{(a-b)^2}{1-\chi c} \right] \right\}^{-1/2}, \quad (4)$$

$$\chi = \frac{\kappa^2 - 1}{\kappa^2 + 1}. \quad (5)$$

The electrostatic part of the inter-particle interaction is based on *linear* quadrupole moments, for which the quadrupole tensor,³⁵ $\underline{\hat{Q}}$, becomes in its eigenbasis

$$\begin{aligned} \underline{\hat{Q}} &= \begin{pmatrix} Q_{xx} & 0 & 0 \\ 0 & Q_{yy} & 0 \\ 0 & 0 & -Q_{xx} - Q_{yy} \end{pmatrix} \\ &= Q \begin{pmatrix} -1/2 & 0 & 0 \\ 0 & -1/2 & 0 \\ 0 & 0 & 1 \end{pmatrix}, \end{aligned} \quad (6)$$

with Q being the strength of the moment.

The interaction between two linear quadrupole moments can be written as^{16,35}

$$\begin{aligned} V_{\text{lr}}(Q^2, \mathbf{r}_{ij}, \hat{\mathbf{u}}_i, \hat{\mathbf{u}}_j) &= \frac{1}{4\pi\epsilon_{\text{pm}}} \frac{3Q^2}{4r_{ij}^5} \\ &\times \left[1 - 5a^2 - 5b^2 - 15a^2b^2 + 2(c - 5ab)^2 \right], \end{aligned} \quad (7)$$

with a , b , and c defined above and ϵ_{pm} being the vacuum permittivity. Even though the interaction decays slower with the distance (i.e., $\sim 1/r^5$) than, e.g., van der Waals interactions

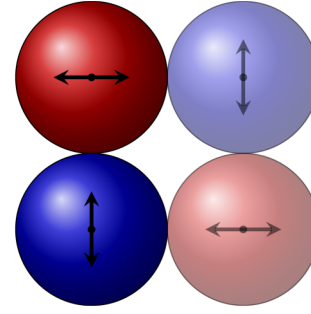


FIG. 2. Typical arrangement of *isolated* quadrupolar particles with weakly anisometric shape (i.e., κ close to unity), induced by the fact that neighboring particles tend to arrange in a mutually orthogonal orientation.

($\sim 1/r^6$) we can still calculate inter-particle energies with sufficient accuracy via a real-space lattice sum. Here we have used a cutoff radius $R_{\text{cut}}/\sigma_0 = 30$ for both, electrostatic and repulsive interactions. The interaction of two linear quadrupoles depends on their respective orientations. In contrast to dipoles, which tend to line up head-to-tail, isolated linear quadrupoles prefer the so-called T-configuration for κ close to unity (see Figure 2). A more detailed discussion of the impact of shape anisotropy on the two-particle arrangement with a minimal electrostatic energy is given in [Appendix A](#).

Throughout, our numerical calculations were performed in the *NPT*-ensemble, where the relevant thermodynamic potential for vanishing temperature is the enthalpy, H ,

$$H = E + PS_0; \quad (8)$$

here E is the internal energy, P is the pressure, and S_0 is the area occupied by the system. Further, we introduce the temperature of the system, T .

Based on the scales of length (σ_0), mass (m_0), and energy (ϵ_0), the quadrupole strength, Q^2 , the pressure P , the temperature T , and the time t are expressed via their respective reduced units, $(Q^*)^2 = Q^2/(4\pi\epsilon_{\text{pm}}\sigma_0^5\epsilon_0)$, $P^* = P\sigma_0^2/\epsilon_0$, $T^* = k_{\text{B}}T/\epsilon_0$ (with k_{B} being the Boltzmann constant) and $t^* = t/\sqrt{\sigma_0^2 m_0/\epsilon_0}$.

III. METHODS AND DATA ANALYSIS

In our approach, we investigate in a *first* step the self-assembly scenarios of our particles at *zero* temperature (i.e., the ground state configurations). This information helps us to classify archetypical particle arrangements (each characterized by a particular spatial and orientational order), which, in turn, help us to understand the strategy of the particles of how to assemble in the energetically most favorable manner. For these investigations, we employ an optimization tool based on evolutionary algorithms, detailed below.

In a *second* step, we take advantage of these ground state configurations and use them as starting configurations in MD simulations, performed at small, but *finite* temperatures. These investigations provide information on the thermodynamic stability of the ordered phases.

A. Evolutionary algorithms

In our effort to identify ground state configurations of our systems, we use an optimization tool based on ideas of EAs.³⁶ EAs are heuristic approaches designed to search for global minima in high-dimensional search spaces and for problems that are characterized by rugged energy landscapes.

In an effort to be compatible with the requirements of an *NPT*-ensemble, we introduce in our approach a unit cell of variable area and shape which creates (together with its periodic images) a system of infinite extent. In the desired configuration (the so-called ground state configuration), particles are located and oriented in this cell in such a way as to minimize the internal energy of the system, which at vanishing temperature is equivalent to the enthalpy.

We initialize the algorithm by creating a set of configurations where particles are located in the cell at random positions and have random orientations. These arrangements are graded by their respective fitness value, a quantity that provides evidence on how suitable this configuration is to solve the optimization problem. Since we are interested in finding ground state structures, a high fitness value of a particular configuration corresponds to a low value of the enthalpy per particle.

Then we iteratively use existing particle arrangements to create new ones by applying one of the two following operations: crossover and mutation. In the former one, we first select two configurations where the choice is biased by high fitness values of the two configurations. Characteristic features of both particle arrangements (such as lattice vectors, particle positions, and particle orientations) are then combined to form a new configuration. The mutation operation, on the other hand, introduces random changes to a randomly chosen configuration, such as moving or rotating an arbitrarily chosen particle or changing the lattice vectors. Typically 2000 iterations are required for a particular state point until convergence towards the global minimum has been achieved.

Our implementation of EAs is memetic, i.e., we combine global and local search techniques: each time a new configuration has been created with one of the two above mentioned EA operations, we apply the L-BFGS-B³⁷ algorithm which guides us to the nearest local minimum.

This algorithm has been applied successfully for a broad spectrum of systems, both in two and three dimensions (see, for instance, Refs. 38–43). Within the context of the present contribution, it should also be mentioned, that a suitable extension of the formalism is also able to cope with long-ranged interactions, as they are encountered in charged systems (see Refs. 44 and 45).

For the present contribution, we have performed with our EA approach computations for 211 evenly spaced values of $\kappa \in [0.4, 2.5]$ and for several combinations of $(Q^*)^2 \in \{0.2, 2, 20\}$ and $P^* \in \{0.1, 1, 10\}$. Due to computational limitations, we have considered unit cells that contain up to twelve particles.

B. Molecular dynamics simulations

In order to investigate structural changes of our system at finite temperature, we perform MD simulations at constant

pressure and temperature for an ensemble of $N = 840$ particles. To this end, we use the Berendsen weak-coupling scheme,⁴⁶ where the classical Newtonian equations of motion are supplemented by terms representing the coupling to a heat- and a pressure-bath.

In the following, we first introduce the translational equations of motion proposed by Berendsen *et al.*,⁴⁶ specializing to the case of a two-dimensional system. Considering a particle with index i ($i = 1, \dots, N$) one has

$$\dot{\mathbf{r}}_i = \mathbf{v}_i + \frac{K}{\tau_P} (\underline{\mathcal{P}} - \underline{\mathbf{P}}) \mathbf{r}_i, \quad (9)$$

$$m_0 \dot{\mathbf{v}}_i = \mathbf{F}_i + m_0 \frac{1}{2\tau_{\text{trans}}} \left(\frac{T}{\mathcal{T}_{\text{trans}}} - 1 \right) \mathbf{v}_i, \quad (10)$$

$$\dot{\mathbf{b}}_\alpha = \left[\frac{K}{\tau_P} (\underline{\mathcal{P}} - \underline{\mathbf{P}}) \right] \mathbf{b}_\alpha. \quad (11)$$

where the vectors \mathbf{b}_α ($\alpha = 1, 2$) define the simulation box and its shape.

In the above equations, the dot represents a time-derivative. Further, \mathbf{r}_i and \mathbf{v}_i denote the position and the velocity of particle with index i , respectively; \mathbf{F}_i is the force on particle i with mass m_0 , and K is the compressibility. The pressure tensors, $\underline{\mathcal{P}}$ (actual pressure) and $\underline{\mathbf{P}}$ (target pressure), are defined below. Further, $\mathcal{T}_{\text{trans}}$ is the actual kinetic temperature, $k_B \mathcal{T}_{\text{trans}} = \sum_i m_i v_i^2 / [2(N-1)]$, where the denominator $2(N-1)$ represents the $2N$ translational degrees of freedom minus two constraints due to momentum conservation in each spatial dimension. To ensure this conservation during the numerical integration, we set the total momentum to zero every 100 time steps.

The (time) constants τ_{trans} and τ_P determine the speed of relaxation of $\mathcal{T}_{\text{trans}}$ and $\underline{\mathcal{P}}$ towards their respective target values defined by the bath. Specifically, the corresponding coupling equations read

$$\dot{\mathcal{T}}_{\text{trans}} = \frac{T - \mathcal{T}_{\text{trans}}}{\tau_{\text{trans}}} \quad \dot{\underline{\mathcal{P}}} = \frac{\underline{\mathbf{P}} - \underline{\mathcal{P}}}{\tau_P}, \quad (12)$$

where the pressure tensors are defined as

$$\underline{\mathcal{P}} = \frac{1}{2S_0} \left[\sum_i m_0 \mathbf{v}_i \otimes \mathbf{v}_i + \sum_{i,j;i < j} \mathbf{r}_{ij} \otimes \mathbf{F}_{ij} \right] \quad \underline{\mathbf{P}} = \frac{1}{2} P \underline{\mathbf{1}}. \quad (13)$$

Here, \otimes denotes the dyadic product of two vectors, S_0 stands for the area of the simulation cell, $\underline{\mathbf{1}}$ is the unit-tensor, and \mathbf{F}_{ij} is the force on particle i exerted by particle j .

To describe the rotational motion of the particles, Eqs. (9)–(13) are supplemented with the following differential equations for the angular velocity, ω_i , of particle i ,

$$\dot{\hat{\mathbf{u}}}_i = \hat{\omega}_i \times \hat{\mathbf{u}}_i + \omega_i \times \hat{\mathbf{u}}_i, \quad (14)$$

$$I \dot{\omega}_i = \mathbf{M}_i + \frac{I}{2\tau_{\text{rot}}} \left(\frac{T}{\mathcal{T}_{\text{rot}}} - 1 \right) \omega_i. \quad (15)$$

Here, \mathbf{M}_i and I are the torque on particle i and the corresponding moment of inertia of particle i , respectively; \times denotes the vector product. The kinetic temperature for the rotation is defined as $k_B \mathcal{T}_{\text{rot}} = \sum_i I \omega_i^2 / N$. This temperature is controlled in analogy to Eq. (12).

To solve the translational equations of motion, i.e., Eqs. (9)–(13) we use a modified leap-frog integrator as proposed in Ref. 46. For the solution of the rotational equations of motion, Eqs. (14) and (15), an analogous procedure is performed (see Ref. 47).

To initialize the particle positions in our system, we use the unit cells obtained from the ground state calculations in the preceding investigations (see Subsection III A). Specifically, we take for each (κ -dependent) ground state the respective unit cell and arrange copies of this cell such that the simulation cell has a minimal circumference. For this simulation cell (which is now defined by the simulation box vectors \mathbf{b}_1 and \mathbf{b}_2) periodic boundary conditions are applied. The pair forces \mathbf{F}_{ij} and torques \mathbf{M}_{ij} are truncated at $R_{\text{cut}} = 6\sigma_0$ and are then shifted in order to make them vanish smoothly.

The MD calculations have been performed at several values of the reduced temperature T^* , that is, $T^* = 0.1, 0.2, \dots, 1.6$. In our simulations, we used a time increment $\Delta t^* = 0.001\,361\,72$ (corresponding at a macroscopic level to $\Delta t \approx 2$ fs). An adequate choice of the time step is imposed by the mass of the particles, for which we have assumed the mass of benzene, $m_0 = 78\text{u}$. Each simulation extends over 210 000 time steps. During the first 20 000 MD steps, the target temperature is gradually increased from $T^* = 0$ towards the respective target value. Structural quantities are then extracted only during the final 10 000 time steps of the simulation. The values for the temperature- and pressure-coupling constants τ_{trans} , τ_{rot} , and τ_P were chosen to be 80 time steps. Of course, the actual volume change of the box is also influenced by the compressibility; its reduced, dimensionless counterpart, $K^* = Km_0^2\sigma_0^2/\epsilon_0$, is set to 0.01. We assume the mass distribution within the particles to be homogeneous and thus obtain for the dimensionless moment of inertia $I^* = 0.25(\kappa + \frac{1}{\kappa})$.

C. Structural analysis — Order parameters

In order to quantify both the positional and the orientational order of the particles, we introduce three different sets of order parameters.

- (i) The *positional* order can be quantified via two-dimensional bond-orientational order parameters (BOOPs),⁴⁸ introducing, in addition, weight factors⁴⁹ that are related to the side lengths of the Voronoi polygon around each particle,

$$\Psi_n = \left\langle \sum_{i=1}^N \frac{1}{\sum_{j \in \mathcal{N}_i} l_{ij}} \left| \sum_{j \in \mathcal{N}_i} l_{ij} \exp(in\phi_{ij}) \right| \right\rangle, \quad (16)$$

here ($j \in \mathcal{N}_i$) indicates that particle j is a nearest neighbor of particle i and l_{ij} is the length of the side of the Voronoi polygon that separates the two particles. ϕ_{ij} is the angle enclosed by the bond between particles i and j and the reference axis, which we choose as the x -axis. For the parameter n , we have chosen the values 4 and 6, highlighting thus via Ψ_4 or Ψ_6 four- or six-fold symmetry, respectively. While BOOPs are calculated for only the best configuration at vanishing temperature, averages

over several configurations are taken in MD simulations, indicated by the brackets in Eq. (16) and in the following.

- (ii) An obvious candidate for quantifying the *orientational* order of the particles is the nematic order parameter S , which is introduced via the tensor order parameter $\underline{\mathbf{T}}$, defined as

$$\underline{\mathbf{T}} = 2 \left\langle \frac{1}{N} \sum_i \hat{\mathbf{u}}_i \otimes \hat{\mathbf{u}}_i \right\rangle - \underline{\mathbf{1}}.$$

S is then simply the positive eigenvalue of the traceless tensor $\underline{\mathbf{T}}$, which can easily be calculated as

$$S = \sqrt{T_{xx}^2 + T_{xy}^2}.$$

The eigenvector associated with S is called the director $\hat{\mathbf{d}}$ and indicates a preferred orientation in the configuration. Note that S is always positive, except in the case that all elements of $\underline{\mathbf{T}}$ vanish: then no preferred direction is present in the system.

A different way of how to measure the orientational order is via the parameter β , defined as

$$\beta = \left\langle \frac{1}{N} \sum_{i=1}^N \frac{1}{\sum_{j \in \mathcal{N}_i} l_{ij}} \sum_{j \in \mathcal{N}_i} l_{ij} |(\hat{\mathbf{u}}_i \cdot \hat{\mathbf{u}}_j)| \right\rangle.$$

- (iii) In addition, a variety of order parameters combining *positional* and *orientational* order can be defined. An example of such an order parameter, which has been used in a previous contribution⁵⁰ is

$$\alpha = \left\langle \frac{1}{2N} \sum_{i=1}^N \frac{1}{\sum_{j \in \mathcal{N}_i} l_{ij}} \sum_{j \in \mathcal{N}_i} l_{ij} |(\hat{\mathbf{u}}_i \cdot \hat{\mathbf{r}}_{ij})^2 + (\hat{\mathbf{u}}_j \cdot \hat{\mathbf{r}}_{ij})^2| \right\rangle.$$

Concluding, we emphasize that orientational order refers to the orientation of the *particles*; the orientation of the linear quadrupolar moment is then imposed by the value of κ : if $\kappa > 1$, then the orientation of the moment is parallel to the main axis of the particles, while for $\kappa < 1$, these two orientations are perpendicular to each other.

IV. RESULTS

A. Ground state configurations

In our discussion of the ground state configurations, we first present the different structural archetypes that we could identify with our EA-approach. We then present the diagram of states: it provides information on the κ -ranges where the respective structures are the energetically most stable ones; we further discuss how the thermodynamic properties and the order parameters of our systems vary over a representative range of κ .

1. Structural archetypes

a. Structures with one preferred orientation. For κ -values both considerably larger or smaller than unity (i.e., by a factor of ≈ 2), the particles tend to align parallel to each other in case of strong anisotropy: they accomplish this by forming tilted rows, characterized by a high density of

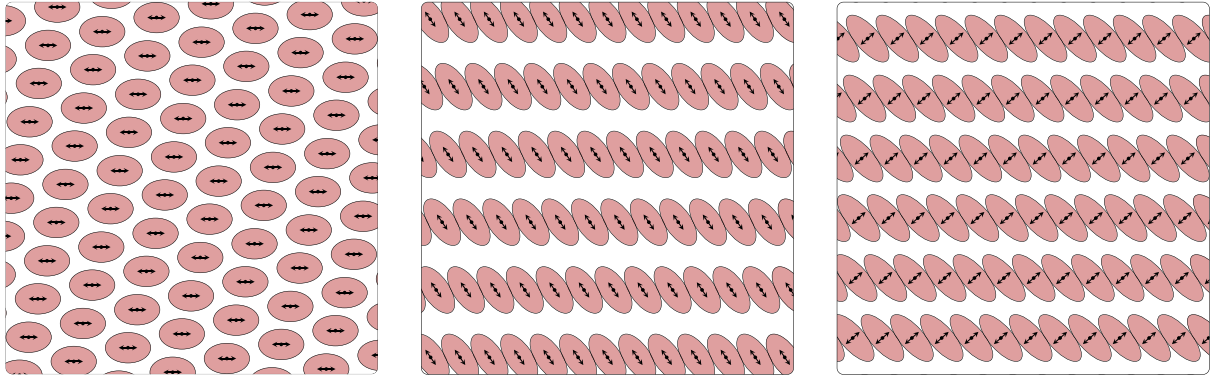


FIG. 3. Taken from Ref. 33. Snapshots of ground state configurations with one preferred particle orientation. Left panel: P-configuration ($(Q^*)^2 = 0$, $P^* = 1$, and $\kappa = 1.5$). Center panel: PD-configuration ($(Q^*)^2 = 2$, $P^* = 1$, and $\kappa = 2.1$). Right panel: PD-configuration ($(Q^*)^2 = 2$, $P^* = 1$, and $\kappa = 0.4$).

particles along these lines; these arrangements are denoted as *parallel displaced*-configurations (“PD;” see Figure 3). Since quadrupolar particles avoid a head-to-tail arrangement, neighboring rows repel each other, inducing thereby large gaps between these lanes; the parallel offset between neighboring rows can be very sensitive to small changes in κ , leading to a slight modulation of the BOOPs as functions of κ (to be discussed below). An interesting special case of this structure is observed for a vanishing quadrupolar moment (i.e., $(Q^*)^2 = 0$), where particles form a distorted hexagonal lattice, denoted as the *parallel*-configuration (“P;” see top left panel of Figure 3).

b. Structures with two preferred particle orientations. Here the preferred structural arrangements are throughout *herringbone*-configurations (“HB”) where particles form alternating, parallel lanes, each of them being characterized by a specific particle orientation: in Figure 4 particles pertaining to different lanes are colored red and blue, respectively. The relative orientation between neighboring particles depends in a highly sensitive manner on κ .

Apart from two special cases (that are encountered for κ -values very close to unity and which will be discussed below) two different versions of the HB-configurations emerge from a closer analysis of the obtained structures.

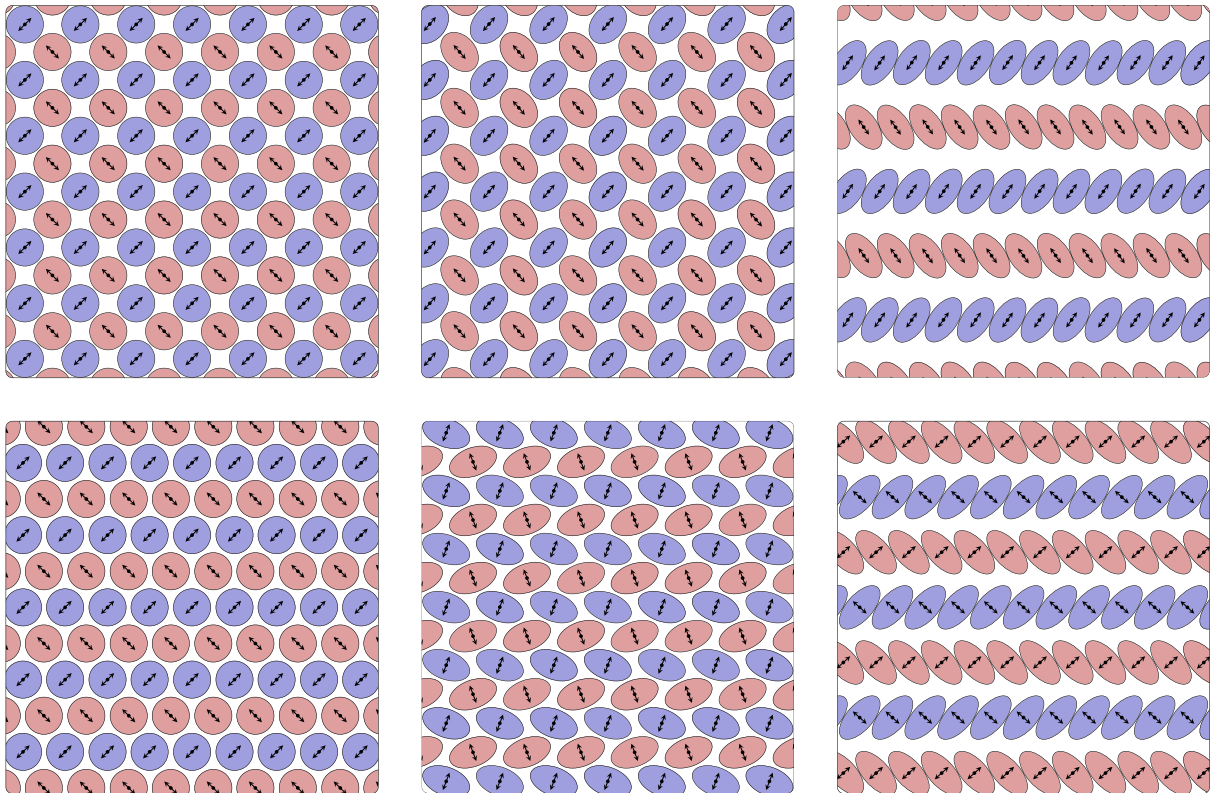


FIG. 4. Taken from Ref. 33. Snapshots of ground state configurations with two preferred particle orientations. Different colors indicate different particle orientations. Left column: top panel — T_{sq} -configuration ($(Q^*)^2 = 2$, $P^* = 1$, and $\kappa = 1$), bottom panel — T_{hex} -configuration ($(Q^*)^2 = 0.2$, $P^* = 10$, and $\kappa = 1$). Center column: top panel — HB_{dense} -configuration ($(Q^*)^2 = 2$, $P^* = 1$, and $\kappa = 1.38$), bottom panel — HB_{dense} -configuration ($(Q^*)^2 = 2$, $P^* = 1$, and $\kappa = 0.58$). Right column: top panel — HB_{loose} -configuration ($(Q^*)^2 = 2$, $P^* = 1$, and $\kappa = 1.83$), bottom panel — HB_{loose} -configuration ($(Q^*)^2 = 2$, $P^* = 1$, $\kappa = 0.48$).

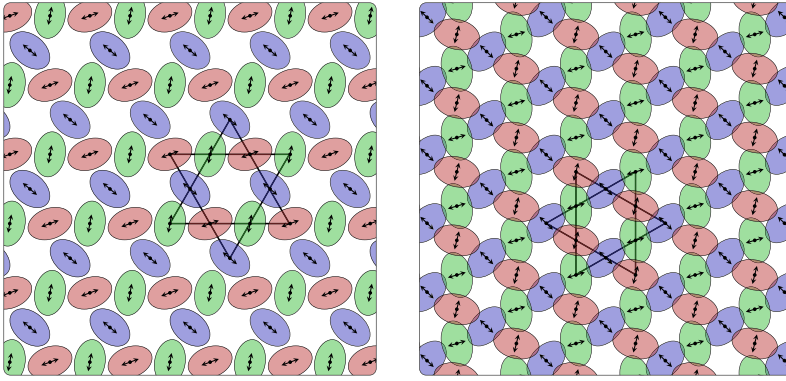


FIG. 5. Taken from Ref. 33. Snapshots of ground state configurations with three preferred particle orientations. Different colors indicate different particle orientations. Left panel: TH-configuration $((Q^*)^2 = 2, P^* = 1, \text{ and } \kappa = 1.5)$, right panel: TH-configuration $((Q^*)^2 = 20, P^* = 1, \text{ and } \kappa = 0.65)$. Lines emphasize underlying triangles and hexagons.

- (i) For κ -values somewhat closer to unity, we observe a rather dense structure, which we denote HB_{dense} -configuration (see panels in the central column of Figure 4).
- (ii) For κ -values that differ more strongly from unity, particles arrange in densely populated rows of alternating orientation (see panels in the right column of Figure 4). Since neighboring rows repel each other, this structure has a lower overall density which we therefore denote as HB_{loose} .

The two special cases of the HB structure mentioned above are observed for κ -values very close to unity where neighboring particles prefer strict mutual orthogonal orientations with respect to their nearest neighbors. (i) For large $(Q^*)^2$ -and small P^* -values, a perfect arrangement of mutually orthogonally oriented particles with an underlying square pattern can be observed, denoted as the *square T*-configuration (“ T_{sq} ,” see left panel of Figure 4). (ii) Further, a closely related arrangement has been identified which is now based on an underlying hexagonal pattern; it is denoted as the *hexagonal T*-configuration (“ T_{hex} ,” see bottom left panel of Figure 4); for this particular configuration, a mutually perfect orthogonal orientation of nearest neighbors can only be realized for $\kappa = 1$.

c. Structures with three preferred particle orientations. A very interesting phenomenon observed in our system is the occurrence of structures where particles arrange in three preferred orientations, characterized by a vanishing nematic order parameter S .

The *spatial* particle arrangement is here — irrespective of the values of Q^* and P^* — reminiscent of a *trihexagonal*

tiling,⁵¹ consisting of regular hexagons that are connected by triangles; we thus denote it as the “TH”-configuration (see Figure 5 where also the hexagons and the triangles are highlighted). Throughout, the relative angle between the orientations of neighboring particles is $\pi/3$, reflected in the order parameter which assumes a value of $\beta = \cos^2(\pi/3) = 1/4$ (see Figure 7).

We note that the occurrence of the TH-configuration strongly depends on the choice of $(Q^*)^2$ and P^* ; in some cases, this particle arrangement is not observed at all (see Figure 8). In contrast, variants of the HB-configuration can almost always be observed in some range of κ (see discussion below).

d. More complicated structures. Using the EA-approach, we also identify more complicated structures, not conforming to the mechanisms described above. These structures require a larger number of particles per cell and turn out to be stable only within very small ranges of κ (see Subsection IV A 2). While we observe several different variants of such particle configurations, they share a common feature, namely, a mesh-like lattice, where chains of particles undulate back and forth (see Figure 6). We denote them as *branched* structures (“B”).

2. Diagram of states

We now discuss the diagram of states which summarizes the occurrence of the previously identified archetypes of ground state configurations of our system for selected values of $(Q^*)^2$ and P^* as we vary κ . Since most of the interesting features of our systems can already be captured in the diagram

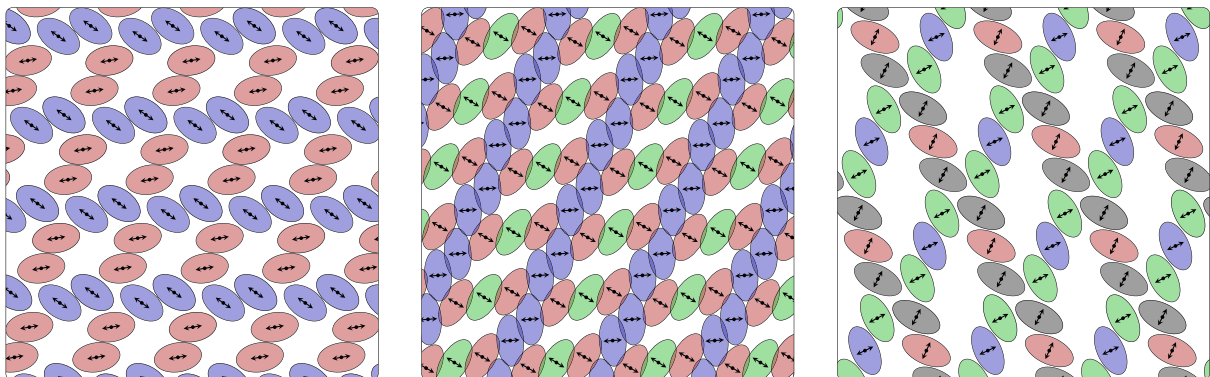


FIG. 6. Taken from Ref. 33. Snapshots of more complicated ground state configurations, so-called B-configurations. Different colors indicate different particle orientations. Left panel: $((Q^*)^2 = 2, P^* = 1, \text{ and } \kappa = 1.66)$, center panel: $((Q^*)^2 = 20, P^* = 10, \text{ and } \kappa = 0.52)$, right panel: $((Q^*)^2 = 2, P^* = 0.1, \text{ and } \kappa = 0.53)$.

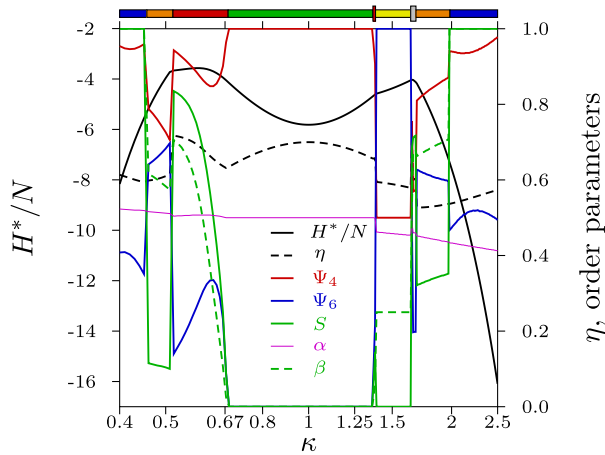


FIG. 7. Taken from Ref. 33. Reduced enthalpy per particle (H^*/N ; left vertical axis) as well as filling fraction η (as defined in the text) and different order parameters (for their definitions see Subsection III C) of the observed ground state configurations (right vertical axis) as functions of κ (as labeled) for $(Q^*)^2 = 2$ and $P^* = 1$. Note the logarithmic scale along the κ -axis. The horizontal bar above the panel specifies the κ -range where the respective ordered structural archetype is the energetically most favorable one via the following color code: T_{sq} (green), HB_{dense} (red), HB_{loose} (orange), PD (blue), TH (yellow), B (grey).

of states obtained for $(Q^*)^2 = 2$ and $P^* = 1$, we focus from now onwards on this particular set of parameters: we present data for the enthalpy and for a selection of appropriate order parameters introduced in Subsection III C that help to identify the respective structures. The filling fraction η , which is also displayed in the following figures, is defined as $\eta = N\pi\sigma_0^2/4/S_0$.

At this point, we remind the reader that the *shape* (and thus the orientation of the particles) is invariant under the transformation $\kappa \leftrightarrow 1/\kappa$ while the relative orientations of the quadrupolar moments for the cases κ and $1/\kappa$ are mutually orthogonal: with this symmetry in mind, we can

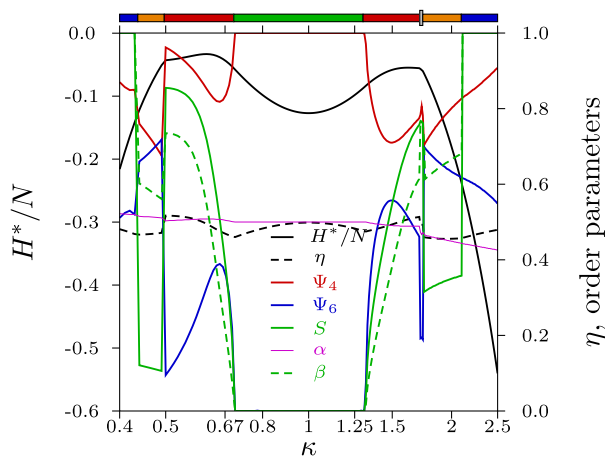


FIG. 8. Taken from Ref. 33. Reduced enthalpy per particle (H^*/N ; left vertical axis) as well as filling fraction η (as defined in the text) and different order parameters (for their definitions see Subsection III C) of the observed ground state configurations (right vertical axis) as functions of κ (as labeled) for $(Q^*)^2 = 0.2$ and $P^* = 0.1$. Note the logarithmic scale along the κ -axis. The horizontal bar above the panel specifies the κ -range where the respective ordered structural archetype is the energetically most favorable one via the following color code: T_{sq} (green), HB_{dense} (red), HB_{loose} (orange), PD (blue), TH (yellow), B (grey).

easily disentangle the impact of $(Q^*)^2$ and P^* on the structure formation by comparing the relevant physical properties for the cases κ and $1/\kappa$. These properties are displayed for $(Q^*)^2 = 2$ and $P^* = 1$ in Figure 7 along with a color-coded, horizontal bar (above this panel) which indicates these κ -ranges where the respective particle configurations are the energetically most favorable ones.

On a qualitative level, we observe that the enthalpy curve is continuous over the entire investigated κ -range; however, it shows kinks at particular values of the aspect ratio which provide a first evidence for the occurrence of discontinuous transitions between the ground state configurations. The specific enthalpy, H^*/N , shows a pronounced local minimum at $\kappa = 1$ (i.e., for circular particle shapes): here the T-configuration is dominant, verified by the fact that in this κ -region $\Psi_4 = 1$ and $\Psi_6 = 0$. In addition, we observe $S = 0$ and $\beta = 0 = \cos^2(\pi/2)$, indicating thereby a relative orthogonal orientation of neighboring particles. In contrast, for more anisometric particle shapes (i.e., small and large κ -values), the enthalpy rapidly decays to rather small values; actually H tends to minus infinity for $\kappa \rightarrow 0$ and $\kappa \rightarrow \infty$ as the quadrupoles start to overlap and the repulsive soft core shrinks as $\sigma_{\perp} \rightarrow 0$. For small and large κ -values, the formation of parallel rows is energetically most favorable and PD-configurations are observed. Here the nematic order parameter S is the appropriate quantity to characterize the emerging structure: indeed, S assumes in these κ -regions the value 1, indicating that a single orientation prevails.

In contrast, for the two intermediate κ -ranges, where the enthalpy assumes local maxima the ground state configurations for κ and $1/\kappa$ are distinctively different; for these κ -values, we observe the formation of more complex structures, reflected by a rather intricate variation of the different order parameters with κ : (i) *Increasing* first κ beyond the region where the T-configuration is stable, the system changes — after a very narrow κ -region where the HB_{dense}-structure occurs — via a discontinuous *structural* transition (identified by a jump in η) into the TH-configuration; the latter one is characterized by $S = 0$, $\Psi_6 = 1$, and $\beta = 0.25 = \cos^2(\pi/3)$ which provides evidence that the difference in orientation angles between nearest neighbors is $\pi/3$. Upon further increasing κ , we pass again a very narrow interval where a branched structure is stable and we eventually reach — again via a discontinuous structural transition — the HB_{loose}-structure; for this configuration, none of the order parameters assume any characteristic value. Eventually we identify for even larger κ -values the aforementioned PD-structure. (ii) *Decreasing*, on the other hand, the value of κ beyond the range where the T-structure is stable, we observe HB-configurations: first the one with the larger density (i.e., the HB_{dense}-structure) and then the HB_{loose}-structure. The shape of β (see Figure 7) indicates that the transition between HB_{dense} and HB_{loose} (and also the subsequent transition to the PD-structure) is of first order, i.e., at some point the relative orientation of neighboring particles is discontinuous.

At this point, it should be mentioned that η and the order parameters do not necessarily behave in the same manner as the system changes from one structure to the other: some order parameters or η may change abruptly, indicating a first

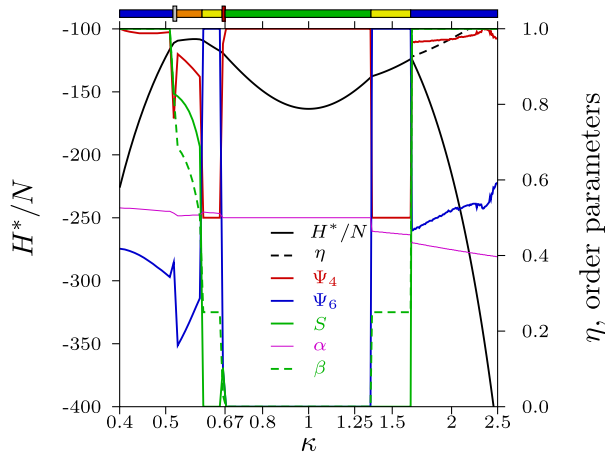


FIG. 9. Taken from Ref. 33. Reduced enthalpy per particle (H^*/N ; left vertical axis) as well as filling fraction η (as defined in the text) and different order parameters (for their definitions see Subsection III C) of the observed ground state configurations (right vertical axis) as functions of κ (as labeled) for $(Q^*)^2 = 20$ and $P^* = 10$. Note the logarithmic scale along the κ -axis. The horizontal bar above the panel specifies the κ -range where the respective ordered structural archetype is the energetically most favorable one via the following color code: T_{sq} (green), HB_{dense} (red), HB_{loose} (orange), PD (blue), TH (yellow), B (grey). Reprinted with permission from M. Antlanger, “Ordered equilibrium structures in systems with long-range interactions,” Ph.D. dissertation (Technische Universität Wien, 2015).

order phase transition, while the other parameters change continuously. As an example, we refer the reader to the transition $HB_{\text{loose}} \rightarrow \text{PD}$ for $\kappa \sim 0.45$.

Another interesting feature emerges as we compare the curves of the order parameters shown in Figure 7 obtained for the parameters $((Q^*)^2, P^*) = (2, 1)$, with the corresponding data calculated for the parameter sets $((Q^*)^2, P^*) = (0.2, 0.1)$ and $((Q^*)^2, P^*) = (20, 10)$, shown in Figures 8 and 9, respectively. The corresponding curves reveal striking similarities, suggesting that appropriate scaling relations of the order parameters via the values of the quadrupole moment and the pressure hold for the respective ground states. In contrast (and interestingly), the enthalpy curves obtained for the different sets of data differ rather substantially in magnitude. We will discuss a possible background scenario of these observations in more detail in Appendix B. There we will show that indeed a scaling relation for the enthalpy of a systems of *hard*, quadrupolar particles can be derived (see Appendix B 1). However, it seems that the softness of our particles — remember that we consider in this contribution particles with a *soft* (albeit rather steep) core — leads to a breakdown of this scaling law. This feature is presumably due to the fact that a simultaneous scaling of the quadrupole moment and of the pressure also induces a change of the density. To take into account this effect properly, we suggest in Appendix C 1 an empirical scaling law for the ground state enthalpy of a system of soft ellipsoidal particles and provide numerical evidence for its justification.

B. Results at finite temperatures

In the current subsection, we analyze the MD results that we have obtained for all considered aspect ratios κ and a set of reduced temperatures T^* . As previously mentioned, the

ground state configurations that we have obtained with the help of the EA for a variety of aspect ratios serve now as initial configurations for the MD simulations. Corresponding snapshots for the most interesting and most representative configurations, obtained after equilibrating the system, are presented in Figure 10.

Before starting the investigations, it is worth to briefly consider typical values of $(Q^*)^2$, P^* in experimental systems. As an example, we consider the quadrupolar Gay-Berne model of benzene proposed by Golubkov and Ren.¹³ We use their quadrupole strength, $Q_{\text{benzene}} = -30.5812 \times 10^{-40} \text{ Cm}^2$, and their spherical diameter, $\sigma_0 \approx 0.307 \text{ nm}$ (the latter value is based on the Gay-Berne contact distance). Using the surface tension of water (the 2D equivalent of pressure) defined in Ref. 52, $P_{\text{water}} = 71.99 \times 10^{-3} \text{ Nm}^{-1}$ at 25 °C, we arrive at the ratio

$$(Q_{\text{benzene}}^*)^2/P_{\text{water}}^* = Q_{\text{benzene}}^2/(4\pi\epsilon_{\text{pm}}\sigma_0^4 P_{\text{water}}) \approx 4.5.$$

However, since the point quadrupole approximation is known to overestimate the interaction strength for narrow interparticle configurations^{13,53,54} due to the singularity in V_{lr} [see Eq. (7)], we consider here a reduced value of $(Q^*)^2/P^* = 2$ instead of 4.5. With this choice, we hope to cover not only benzene molecules but also other quadrupolar molecules. By identifying $P^* = 1$ with P_{water} , we arrive at the following energy scale $\epsilon_0 = P_{\text{water}}\sigma_0^2/P^* = P_{\text{water}}\sigma_0^2 = 4.09 \text{ kJ/mol}$. In the following, we present MD simulation results for the parameter pairs $((Q^*)^2, P^*) = (2, 1)$, and $(4, 2)$. We start with a detailed investigation of the structure at $(Q^*)^2 = 2$, $P^* = 1$ and different temperatures.

The MD simulations reveal that the structures predicted for vanishing temperature remain stable also at low temperature ($T^* = k_{\text{B}}T/\epsilon_0 = 0.2$, see panels in the second column of Figure 10). As T^* increases monotonously, defects start to form (see panels in the third column of Figure 10): the most common of these is a slight wavelike modulation of previously straight lines. Finally, once the temperature has been raised above a certain threshold value (see panels in the fourth column of Figure 10), the crystalline order is rapidly lost. The corresponding transition temperatures depend strongly on κ : configurations with $\kappa \approx 1$ (T_{sq} -configuration) and κ far from unity (PD-configuration) turn out to be the most stable ones: in this situation, particles can approach very closely and exert thus a strongly attractive quadrupole-quadrupole interaction; these ordered structures break up only at temperatures as high as $T^* = 1.1$ and $T^* = 1.2$, respectively. In contrast, the rather complicated B-configurations melt already at temperatures as low as $T^* = 0.5$ (with $\kappa = 1.66$).

In order to investigate and to locate the transition of the system from the ordered to the disordered regime, we focus in the following on the reduced potential energy, E_{pot}^* , and the reduced system area, S_0^* (in units of ϵ_0 and σ_0 , respectively). Figure 11 depicts E_{pot}^* and S_0^* as functions of the reduced temperature T^* for all considered values of the aspect ratio κ . Upon increasing the temperature, E_{pot}^* progressively decreases in magnitude and finally approaches zero, reflecting the diminishing role of particle interactions. At the same time, the area S_0^* increases. Interestingly, we

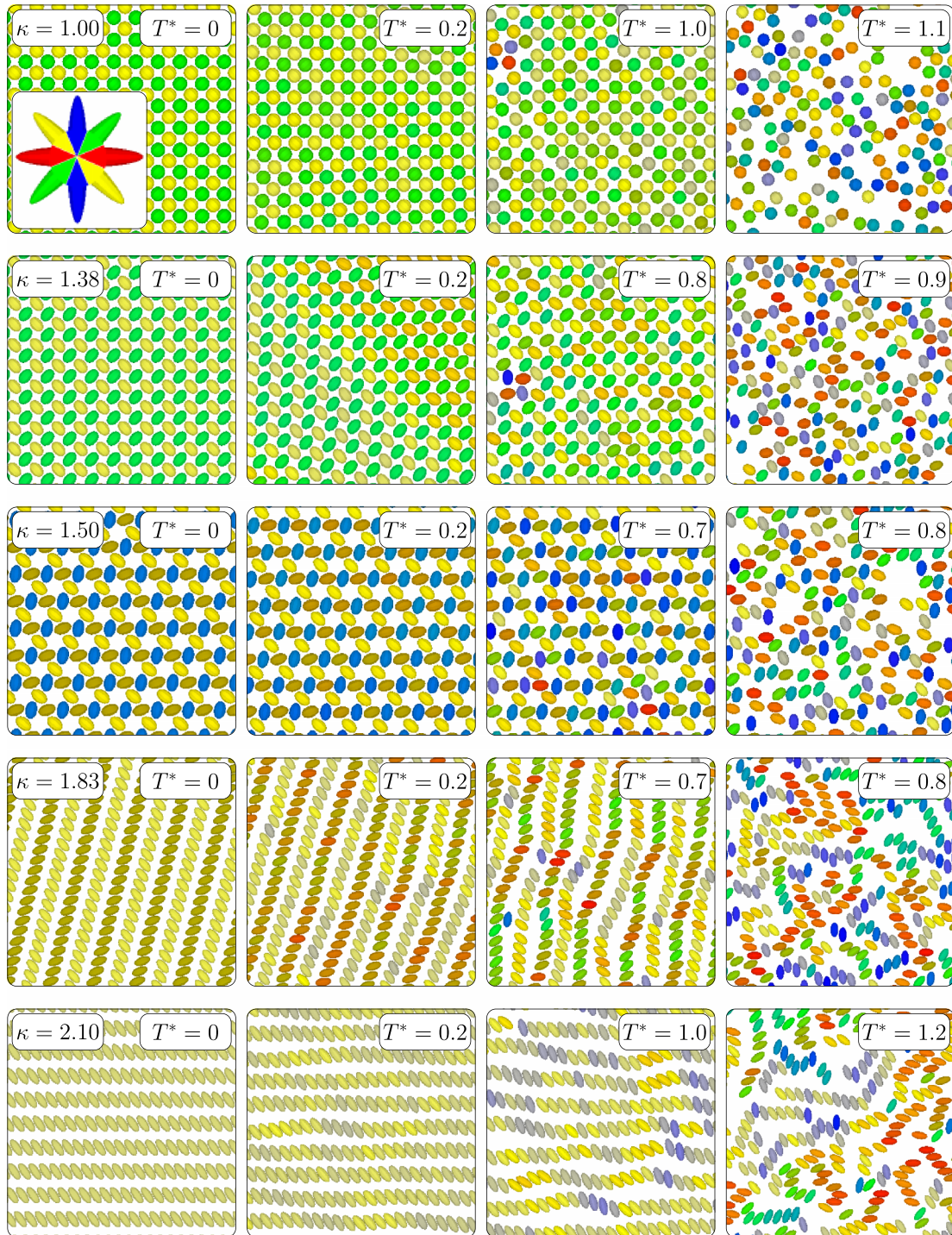


FIG. 10. Snapshots of equilibrated particle configurations as obtained in MD simulations for different values of $\kappa = \sigma_{\parallel}/\sigma_{\perp}$ (along rows; as labeled) and $T^* = k_B T / \epsilon_0$ (along columns; as labeled). Different colors indicate different particle orientations (see colour scheme in the inset of the top left panel). First row: $\kappa = 1$ (T_{sq} -configuration); second row: $\kappa = 1.38$ (HB_{dense} -configuration); third row: $\kappa = 1.5$ (TH -configuration); fourth row: $\kappa = 1.83$ (HB_{loose} -configuration); fifth row: $\kappa = 2.1$ (P -configuration). Configurations for $T^* = 0$ have been obtained via the EA route.

observe along this process that both $E_{\text{pot}}^*(T^*)$ and $S_0^*(T^*)$ show discontinuous changes within very small temperature intervals for all κ -values investigated; these “jumps” are found for both quantities at approximately the same temperature. We attribute these observations to the occurrence of a first order phase transition. The temperatures that delimit these intervals are marked in Figure 11 by contour lines as functions of κ . Only for $\kappa \approx 1.66$, no such discontinuity in $E_{\text{pot}}^*(T^*)$ could be resolved;

this fact can be related to the finite size of the temperature grid. Intentionally, we have not evaluated the susceptibility, since it is well established that energy fluctuations are not correctly reproduced within the Berendsen scheme.^{55,56}

We now arrive at the discussion of the previously defined BOOPs Ψ_4 and Ψ_6 [see Eq. (16)]; they are displayed in Figure 12. As already shown in Figure 7, we find for all our ground state configurations intervals in κ where at least

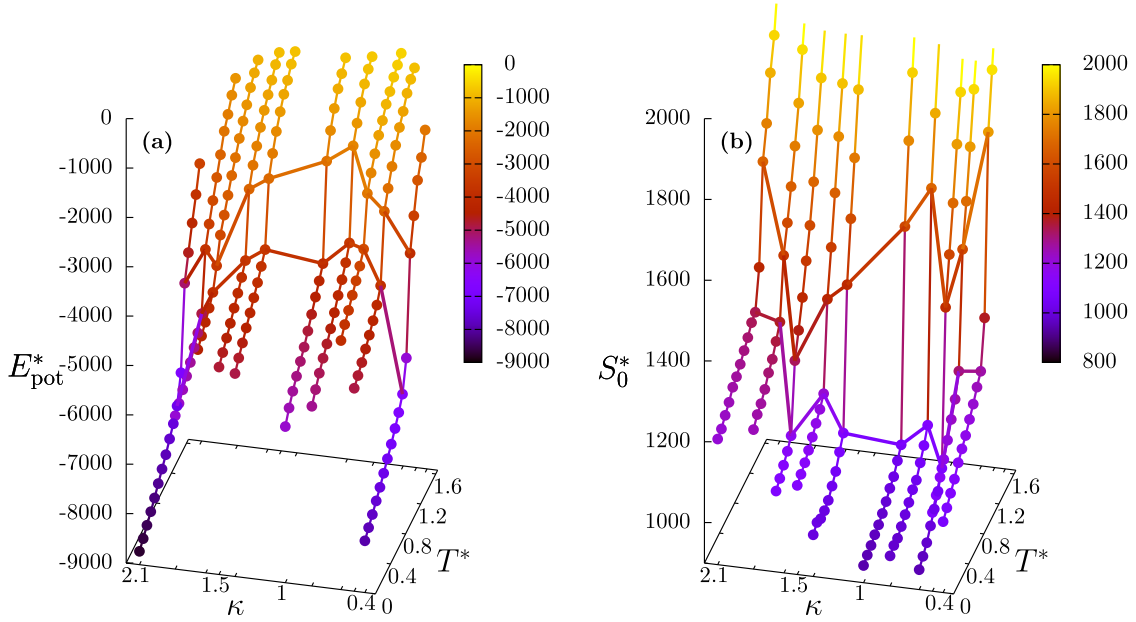


FIG. 11. Reduced, dimensionless potential energy, E_{pot}^* (left panel), and dimensionless system area, S_0^* (right panel), as functions of the temperature, T^* , and of the aspect ratio, κ . The color code of these quantities is shown on the right hand side of each panel. Each symbols represents a state point investigated in an MD run; symbols are connected by lines as guides to the eye. The contour lines are explained in the text.

one of the two parameters does not vanish. Considering now the temperature dependence of these quantities, we observe for all κ -values investigated a discontinuous change of both Ψ_4 and Ψ_6 (if not zero in the ground state) at exactly the same temperatures where a discontinuous change in S_0^* was observed. To analyze the structure of the system at

finite temperatures on an even more quantitative level, we have calculated in addition various coefficients of the pair distribution function in an expansion in terms of rotational invariants. To be more specific, we use a two-dimensional version of the three dimensional coefficient functions of the pair distribution function,⁵⁷ i.e.,

$$g^{l_1 l_2 l}(R) = \left\langle \frac{S_0}{N(N-1)2\pi R} \sum_i \sum_{j \neq i} \psi^{l_1 l_2 l}(\hat{\mathbf{r}}_{ij}, \hat{\mathbf{u}}_i, \hat{\mathbf{u}}_j) \delta(|\mathbf{r}_{ij}| - R) \right\rangle, \quad (17)$$

where the $\psi^{l_1 l_2 l}(\hat{\mathbf{r}}_{ij}, \hat{\mathbf{u}}_i, \hat{\mathbf{u}}_j)$ are rotational invariants. Here we focus on the coefficients $g^{000}(R)$, $g^{220}(R)$, and $g^{202}(R)$ defined via the following two-dimensional rotational invariants:

$$\psi^{000} = 1 \quad \psi^{220} = 2(\hat{\mathbf{u}}_i \cdot \hat{\mathbf{u}}_j)^2 - 1 \quad \psi^{202} = 2(\hat{\mathbf{u}}_i \cdot \hat{\mathbf{r}}_{ij})^2 - 1. \quad (18)$$

The function $g^{000}(R)$ corresponds to the familiar pair correlation function. The other functions, $g^{202}(R)$ and $g^{220}(R)$, describe, in addition, a local orientational order of the particles. Similar to 3D systems,⁵⁸ we can interpret these coefficients as follows: $g^{220}(R)$ provides information about the conditional probability density of a particle (relative to the bulk probability density) whose orientation axis is aligned in parallel (positive value) or orthogonal (negative value) to the orientation axis of a considered particle; $g^{202}(R)$ describes the conditional probability density of a particle (again, relative to the bulk probability density) positioned along or aside the axis of a considered particle.

In the panels of Figure 13, we present numerical results for these three functions for $\kappa = 2.1$ (see also the corresponding snapshots shown in the panels in the bottom row of Figure 10). For all three correlation functions, the first peak is located at around $0.8\sigma_0$: this position does not exactly mark the face-to-face alignment of the particles (which occurs at $\sim 0.69\sigma_0$) and thus provides evidence for a slightly shifted parallel configuration, induced by the quadrupole (see snapshots shown in the panels of the bottom row in Figure 10). For $T^* = 1.2$, we observe a rapid decay of $g^{000}(R)$ towards unity for large particle distances R : the crystalline order has completely vanished, reflected by the missing peaks for larger R -values. Since at low temperatures all particles are oriented in the same direction, $g^{220}(R)$ is equivalent to $g^{000}(R)$; however, as the temperature attains $T^* = 1.2$, we observe that for large R -values the orientational order is lost and thus $g^{220}(R)$ vanishes already at $R \approx 2\sigma_0$. Finally, $g^{202}(R)$ oscillates around zero in the ordered phase for low temperatures ($T^* < 1.2$) due to the fact that $g^{202}(R)$ is — by definition — not able

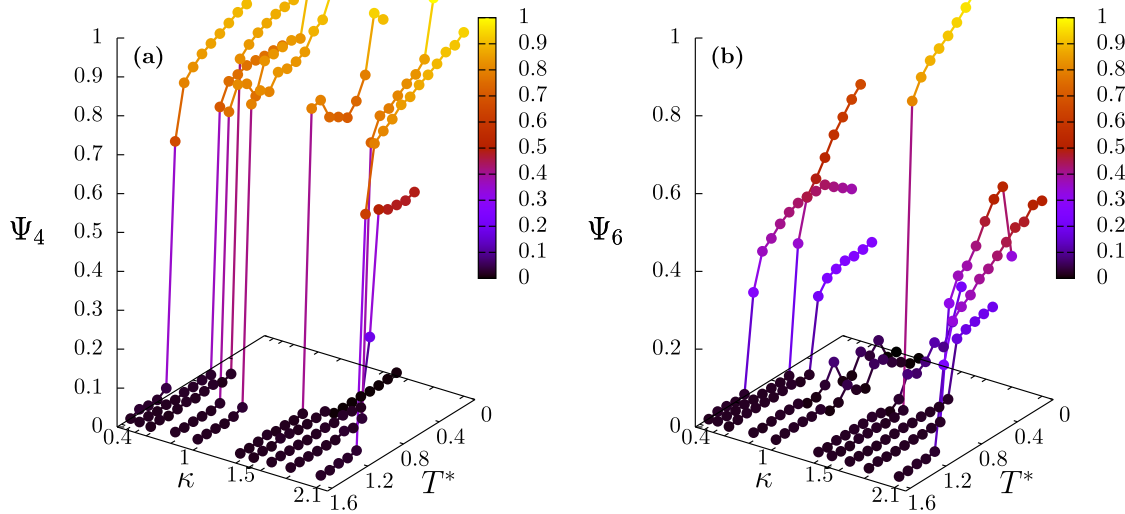


FIG. 12. Bond orientational order parameters Ψ_4 (panel (a)) and Ψ_6 (panel (b)) as functions of κ for different temperatures T^* . The color code of these quantities is shown on the right hand side of each panel. Each symbols represents a state point investigated in an MD run; symbols are connected by lines as guides to the eye.

to contribute to the overall particle density. For $T^* \gtrsim 1.2$, $g^{202}(R)$ completely vanishes for large R -values ($R \gtrsim 2\sigma_0$): obviously, a loss of orientational order occurs for $T^* \gtrsim 1.2$. This temperature threshold, which can be interpreted as a

melting temperature, agrees fairly well with the temperature where the discontinuous changes in $E_{\text{pot}}^*(T^*)$ and $S_0^*(T^*)$ (see Figure 11) and in the BOOPs (see Figure 12) were observed. Concluding, we note that related investigations carried out for other κ -values led to analogous conclusions about the corresponding melting temperature.

These observations motivate investigations on a *melting curve* that separates the ordered from the disordered phase as we increase the temperature. This line is displayed in Figure 14 for all considered aspect ratios κ . We emphasize that these data represent only an estimate for the true, two-phase coexistence lines characterizing a first-order transition. For the latter, one would also expect the occurrence of a hysteresis, i.e., the observation of two different curves, depending on whether the system is heated up or cooled down from a low or a high-temperature state, respectively. We briefly come back to this issue below. Another interesting feature of the melting curve that can be observed is that it exhibits some degree of symmetry in shape when exchanging κ and $1/\kappa$ (see Figure 14). Of course, we would not expect full symmetry since the electrostatic properties for the cases κ and $1/\kappa$ are different (see bottom panels in Figure 1). From the data, we can conclude that for particles with large eccentricities the melting occurs at higher temperatures than for κ -values close to unity.

Given the large amount of numerical calculations required to construct the melting line in Figure 14, which was calculated for one particular set of parameters, $(P^*, (Q^*)^2)$, it would be obviously desirable and helpful to have a scaling relation at hand which allows to easily obtain (or to extrapolate) corresponding melting lines for other parameter sets. In Appendix B 2, we show that such a relation does indeed exist for *hard* particles. This relation states that the probability to encounter a microscopic configuration of the many-particle system in phase space is invariant under the simultaneous transformations $Q^2 \rightarrow \mu Q^2$, $P \rightarrow \mu P$, $T \rightarrow \mu T$, with μ being a scaling factor. However, in this contribution, we consider

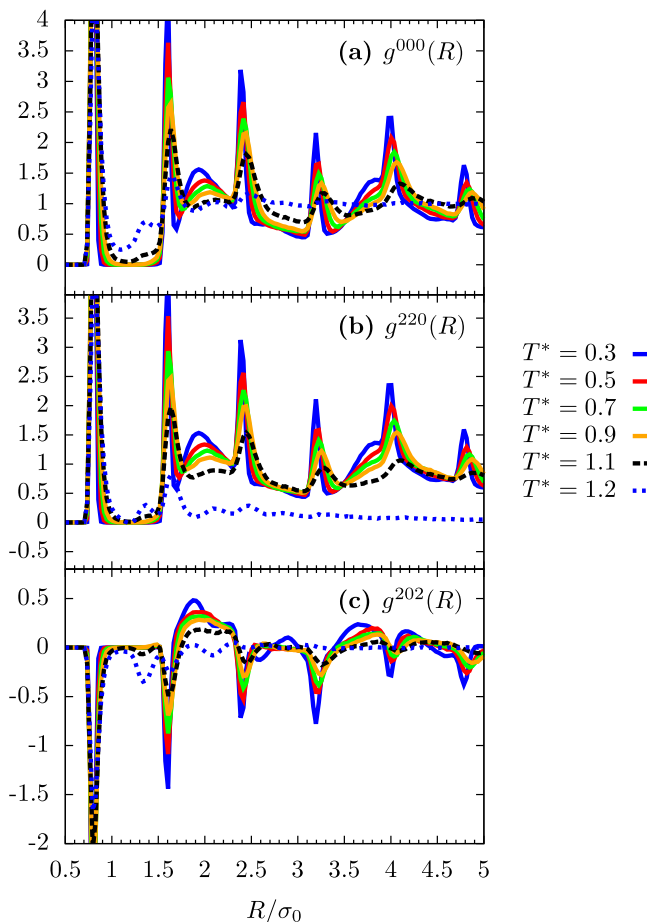


FIG. 13. Correlation functions $g^{000}(R)$ —panel (a), $g^{220}(R)$ —panel (b), and $g^{202}(R)$ —panel (c) for $\kappa = 2.1$ and various temperatures (as labeled).

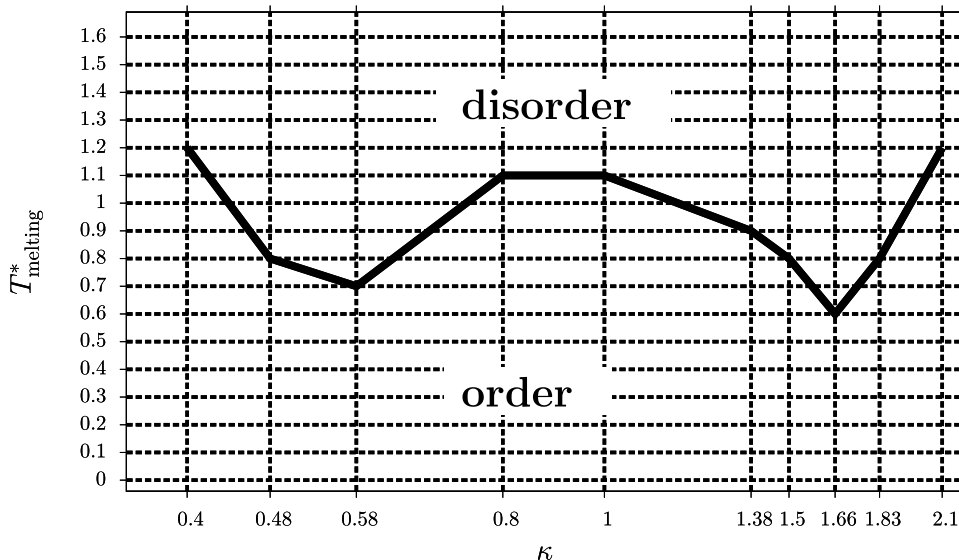


FIG. 14. Estimate of the melting curve T_{melting}^* ($(Q^*)^2 = 2, P^* = 1, \kappa$) that separates the ordered phase (at low temperatures) from the disordered phase (at high temperatures); for details cf. text. Data along on the line correspond to results obtained for disordered state points.

soft particles (even though characterized by a rather harsh repulsion, see Eq. (2)). Nevertheless, as we discuss in Appendix C 2, it is also possible for the system at hand to provide via a suitably adapted scaling law a rough estimate of the location of the melting line at scaled parameters.

Finally and for the sake of completeness, we now discuss our investigations on the melting transition as obtained in a cooling process (“simulated annealing”). The central question that we address is whether the ground state structures can be reproduced — at least locally — with MD simulations starting from a disordered phase at higher temperatures. To this end, we performed simulations at $(Q^*)^2 = 2$ and several values of κ , initializing the system with random particle positions

and orientations and cooling it down gradually. The initial pressure and temperature were set to $P^* = 10$ and $T^* = 5$, respectively; the initial box-shape is quadratic with a side length of $50\sigma_0$. Within the first 200 000 MD steps we linearly decreased the pressure and the temperature down to $P^* = 1$ and $T^* = 0.1$, respectively. The simulations extended in total over 410 000 MD steps. For the other simulation parameters, we refer the reader to Sec. III B. Our data provide evidence that the predicted ground state could be obtained via this simulated annealing process only for very few state points. In general, the formation of ordered structures via such a process is hampered and delayed by frustration effects, especially for κ -values far from unity, where particles encounter — due to their elongated shapes — difficulties to rotate. As an example, we discuss the pair correlation function $g^{000}(R)$, obtained for $\kappa = 0.8$ (i.e., a value close to unity) and depicted in Figure 15(a). We observe a coincidence in the peak positions of $g^{000}(R)$, but not in their heights. We interpret this deviation as an artefact of the crystallite structure appearing after cooling (see Figure 15(b) and 15(c)). This might be a consequence of the lack of long-range order in 2D systems.

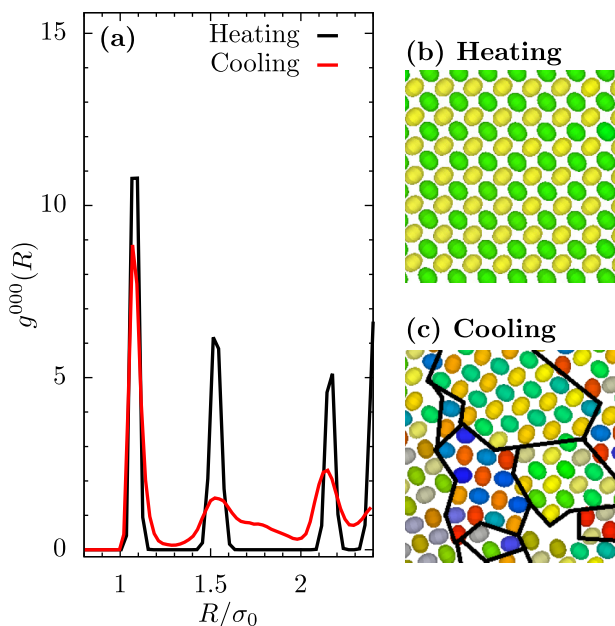


FIG. 15. Pair correlation function $g^{000}(R)$ (panel (a)) for a system with $\kappa = 0.8$ at a temperature $T^* = 0.1$, pressure $P^* = 1$, and quadrupole strength $(Q^*)^2 = 2$ after a melting (snapshot in panel (b)) and a cooling procedure (snapshot in panel (c)). For the color code of the snapshots see inset in Figure 10.

V. CONCLUSIONS

In summary, we have proposed a simple model that mimics the essential features of elongated, organic molecules without a net charge or dipole moment: it consists of soft ellipsoids with an embedded linear quadrupole moment. The preferred orthogonal arrangement of linear quadrupole moments in close proximity to each other represents an interesting contrast as compared to dipolar systems, where particles prefer parallel arrangements, thus often forming chains. The self-assembly scenarios of our system result from a competition between the shape anisotropy of the ellipsoids and the quadrupolar interactions.

Operating in the NPT ensemble, we have investigated the system for numerous different sets of system parameters, $(Q^*)^2$ and P^* , and could identify different strategies of the

system, depending on the shape anisotropy κ . While we always observed configurations of parallel rows of particles for κ -values far from unity, the sequence of structures between these two limiting cases strongly depends on the competition between the short-ranged and the long-ranged, electrostatic contributions to the interaction. For $\kappa \approx 1$, we observe two different configurations with orthogonal particle arrangement, one of them based on a square lattice, the other closely related to a hexagonal lattice. Intermediate ranges of κ — both for $\kappa > 1$ as well as for $\kappa < 1$ — are mostly dominated by two variations of the herringbone structure. In addition, we observe for selected κ -values a non-trivial lattice, closely related to the trihexagonal tiling. In very small ranges of κ , more complicated, branched structures can emerge. However, these turn out to be in general rather unstable at finite temperatures, as shown in complementary MD simulations: thus we speculate that they are metastable at vanishing temperature.

For future work, it would be useful to extend our simple model in two directions: (i) the particles interaction should include a general quadrupole moment and (ii) the system could be confined to a slab geometry or be extended to full three dimensions. These extensions would nicely meet the considerable experimental interest in the self-assembly of complex organic molecules on surfaces.^{59,60} Some of these systems show a remarkable variety of different structures, which can even be controlled via external parameters such as magnetic fields⁶¹ or light with different polarization,⁶² opening thereby the route to many interesting technological applications.^{63–68} The understanding of our simple model considered in the present contribution could serve as a suitable starting point for related investigations of the more complex molecules considered in these studies. Extending the model step-by-step towards more complicated shapes and to more intricate effective interactions would help to understand the numerous competing effects.^{5,69}

Finally we note that so-called Inverse Patchy Colloids (IPCs),⁷⁰ i.e., colloids decorated with charged patches, represent due to their charge distribution a closely related system, as they also carry a linear quadrupole moment. IPCs have been observed to form similar structures as the ones encountered here both in simulations^{71,72} as well as in experiments.⁷³

ACKNOWLEDGMENTS

This work was supported by the Deutsche Forschungsgemeinschaft (DFG) within the framework of the CRC 951 (Project No. A7). M.A. and G.K. gratefully acknowledge financial support by the Austrian Science Foundation (FWF) under Project Nos. P23910-N16 and F41 (SFB ViCoM), and by E-CAM, an e-infrastructure centre of excellence for software, training, and consultancy in simulation and modelling funded by the European Union (Project No. 676531). Further, financial support from the bilateral projects PHC-Amadeus-2012 and 2015 (under Project Nos. 26996UC and 33618YH), Projekt Amadée (under Project Nos. FR 10/2012 and FR 04/2015), the German Academic Exchange Service (DAAD — under Project No. 10041371), the bilateral

projects PHC-Procopé-2013 (under Project No. 28400PD), and funding by Investissement d’Avenir LabEx PALM (Grant No. ANR-10-LABX-0039) is acknowledged.

APPENDIX A: TWO PARTICLE GROUND STATE CONFIGURATIONS AT PARTICLE CONTACT

We consider two quadrupolar particles at contact, i.e., $r_{12} = \sigma(\hat{\mathbf{r}}_{12}, \hat{\mathbf{u}}_1, \hat{\mathbf{u}}_2)$ [see Eq. (4)] and optimize their respective and relative orientations by minimizing their electrostatic energies. In Figure 16, we display the angles α_1 and α_2 , enclosed by the vector connecting the centers of the two particles and the orientations of the respective quadrupolar moments in the corresponding optimal configurations, as functions of κ (for the definitions of the angles see also inset in Figure 16). Obviously, the T-configuration is only stable for values of κ close to unity. For strong anisometry ($\kappa \lesssim 0.75$ or $\kappa \gtrsim 1.2$), the ground state configuration is parallel displaced (PD).

APPENDIX B: REDUCTION OF PARAMETER SPACE FOR HARD PARTICLES

The goal of the present subsection is to derive scaling relations for the system parameters Q^2 (quadrupole strength) and P (pressure) under which the thermodynamic properties of the system (and thus its ground state configurations) remain unchanged. Of course, these relations also hold for our reduced parameters, which we introduced at the end of Sec. II.

We assume in the following a simplified version of our interaction potential, namely the *quadrupolar hard-ellipse* (QHE) model, defined by its interaction

$$V_{\text{QHE}}(\mathbf{r}_{ij}, \hat{\mathbf{u}}_i, \hat{\mathbf{u}}_j; Q^2) = \begin{cases} V_{\text{tr}}(\mathbf{r}_{ij}, \hat{\mathbf{u}}_i, \hat{\mathbf{u}}_j; Q^2) & r_{ij} > \sigma(\mathbf{r}_{ij}, \hat{\mathbf{u}}_i, \hat{\mathbf{u}}_j) \\ \infty & \text{else} \end{cases}, \quad (\text{B1})$$

where $\sigma(\mathbf{r}_{ij}, \hat{\mathbf{u}}_i, \hat{\mathbf{u}}_j)$ has been defined in Eq. (4). Thus, contrary to our original system (see Sec. II), the QHE model consists of *impenetrable* ellipsoidal particles, whereas the quadrupolar, long-range part of the interaction is identical to our original model, Eq. (7).

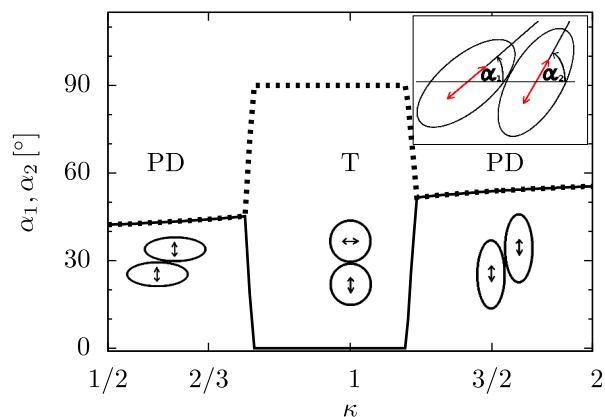


FIG. 16. Angles α_1 (full line) and α_2 (broken line) as functions of κ that specify the energetically most favorable configuration of two quadrupolar particles in direct contact (see text and the inset for visualization). Note the logarithmic scale along the κ -axis.

The potential energy, E_{pot} , of a specific configuration of the QHE system is defined via

$$E_{\text{pot}}(\mathbf{r}^N, \hat{\mathbf{u}}^N; Q^2) = \sum_{i,j;i < j} V_{\text{QHE}}(\mathbf{r}_{ij}, \hat{\mathbf{u}}_i, \hat{\mathbf{u}}_j; Q^2), \quad (\text{B2})$$

where $\mathbf{r}^N = (\mathbf{r}_1, \dots, \mathbf{r}_N)$ and $\hat{\mathbf{u}}^N = (\hat{\mathbf{u}}_1, \dots, \hat{\mathbf{u}}_N)$ specify the microscopic configuration of the particles.

1. Ground state (vanishing temperature)

At vanishing temperature, the particles are positioned and oriented in a non-degenerate ground state in an NPT ensemble such that the enthalpy, H , is minimal, that is

$$H = \min_{\{\mathbf{r}^N, \hat{\mathbf{u}}^N, S_0\}} [E_{\text{pot}}(\mathbf{r}^N, \hat{\mathbf{u}}^N; Q^2) + PS_0]. \quad (\text{B3})$$

The scaling properties of the QHE interaction potential (via Eq. (B1)), with the quadrupole strength Q^2 induces a scaling property of the entire potential energy [cf. Eq. (B2)], i.e., $E_{\text{pot}}(\mu Q^2) = \mu E_{\text{pot}}(Q^2)$; henceforward, μ is a simple scaling parameter. Since the enthalpy H is a linear combination of E_{pot} and P , replacing Q^2 by μQ^2 [cf. Eq. (B3)] leads to the same ground state only if the pressure also scales with μ . Thus, we can conclude that a particular ground state configuration of the QHE model (specified by $\{\mathbf{r}_{\text{GS}}^N, \hat{\mathbf{u}}_{\text{GS}}^N, S_0^{\text{GS}}\}$) remains invariant under the transformations $Q^2 \rightarrow \mu Q^2$ and $P \rightarrow \mu P$.

2. Finite temperatures

We next consider the QHE system at $T > 0$. The phase space probability for the occurrence of a microscopic configuration (specified by $\{\mathbf{r}^N, \hat{\mathbf{u}}^N\}$) in a phase space volume of infinitely small extent in an NPT-ensemble is given by

$$\begin{aligned} & \rho(\mathbf{r}^N, \hat{\mathbf{u}}^N, S_0) d\mathbf{r}^N d\hat{\mathbf{u}}^N dS_0 \\ &= \frac{1}{Z_{\text{conf}}} \exp\{-(k_B T)^{-1} [E_{\text{pot}}(\mathbf{r}^N, \hat{\mathbf{u}}^N; Q^2) + PS_0]\} \\ & \times d\mathbf{r}^N d\hat{\mathbf{u}}^N dS_0, \end{aligned} \quad (\text{B4})$$

where Z_{conf} is the corresponding partition function of the ensemble. It is obvious that Eq. (B4) is invariant under the transformations $E_{\text{pot}} \rightarrow \mu E_{\text{pot}}$, $P \rightarrow \mu P$, and $T \rightarrow \mu T$. Since we know from Eqs. (7) and (B2) that the potential energy of non-overlapping, impenetrable particles is proportional to Q^2 , i.e.,

$$E_{\text{pot}} = \sum_{i,j;i < j} V_{\text{QHE}}(\mathbf{r}_{ij}, \hat{\mathbf{u}}_i, \hat{\mathbf{u}}_j; Q^2) \propto Q^2, \quad (\text{B5})$$

we obtain the simple rule, that $\rho(\mathbf{r}^N, \hat{\mathbf{u}}^N, S_0)$ is invariant under the scaling law $Q^2 \rightarrow \mu Q^2$, $P \rightarrow \mu P$, and $T \rightarrow \mu T$.

Thus, if we have a reference system (specified by Q^2 , P , and T) at hand, we can simply calculate the properties of another system (index “new”) via the following procedure. Given the size of the corresponding molecule, σ_{new} , its aspect ratio κ and the quadrupole strength, Q_{new}^2 , it is thus possible to estimate the order-disorder transition temperature for the new system: we first calculate the reduced quadrupole strength via $(Q_{\text{new}}^*)^2 = Q_{\text{new}}^2 / (4\pi\epsilon_{\text{pm}}\sigma_{\text{new}}^5\epsilon_0)$ from which we obtain the scaling factor μ from $\mu = (Q_{\text{new}}^*/Q^*)^2$. The order-disorder temperature and pressure of the new system then follow from

the corresponding quantities of the reference system, T_{melting}^* and P , via $T_{\text{melting,new}}^* = \mu T_{\text{melting}}^*$ and $P_{\text{new}}^* = \mu P^*$.

APPENDIX C: APPLICABILITY OF PARAMETER SCALING FOR SOFT PARTICLES

We now explore to which extent we can apply the parameter scaling relations derived for the QHE system to the actual system of soft particles investigated in the main part of this paper (see Sec. II).

1. Ground state (vanishing temperature)

The total potential energy for a specific configuration of soft quadrupolar ellipsoids is defined through

$$\begin{aligned} E_{\text{pot}}(\mathbf{r}^N, \hat{\mathbf{u}}^N; Q^2) &= \sum_{i,j;i < j} V_{\text{sr}}(\mathbf{r}_{ij}, \hat{\mathbf{u}}_i, \hat{\mathbf{u}}_j) \\ &+ V_{\text{r}}(\mathbf{r}_{ij}, \hat{\mathbf{u}}_i, \hat{\mathbf{u}}_j; Q^2). \end{aligned} \quad (\text{C1})$$

As pointed out in the discussion of the ground states in Sec. IV A, the order parameters reveal as functions of κ strong similarities when one compares their values as obtained for the parameter sets $((Q^*)^2, P^*) = (0.2, 0.1)$ and $((Q^*)^2, P^*) = (20, 10)$. This suggests that the soft particle system fulfills at $T = 0$ a similar scaling relation as the QHE system.

However, the corresponding enthalpy curves match only in terms of shape, but not in terms of magnitude. We thus introduce a *phenomenological* correction to the simple scaling law of the enthalpy as developed in Appendix B 1. Specifically, we assume that a scaling of P and Q^2 with a factor μ results in a small rescaling of the ground state coordinates, i.e., $\mathbf{r}_i \rightarrow \gamma \mathbf{r}_i$, where γ attains values close to unity. We further assume that, when passing from one ground state, obtained for parameters (Q^2, P) and a filling fraction η , to a new ground system (index “new”), specified by parameters $(\mu Q^2, \mu P)$ and a filling

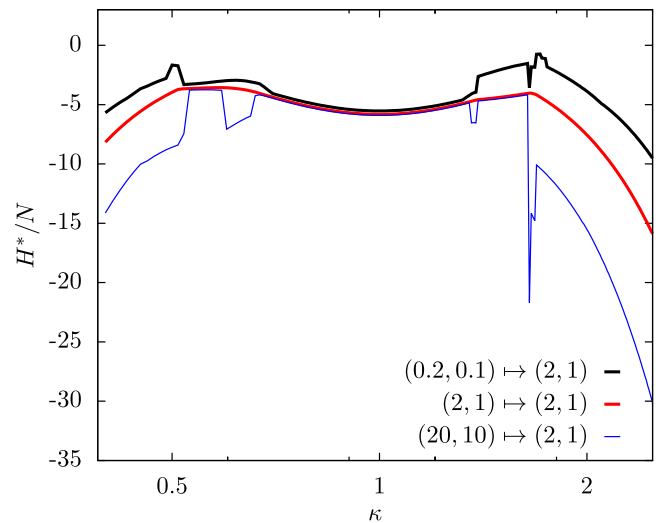


FIG. 17. Reduced, dimensionless enthalpy curves obtained for the parameter sets $((Q^*)^2 = 0.2, P^* = 0.1)$ and $((Q^*)^2 = 20, P^* = 10)$, mapped via the scaling laws presented in the text (cf. Eq. (C4)) onto the enthalpy, calculated directly for the set of parameters $((Q^*)^2, P^*) = (2, 1)$.

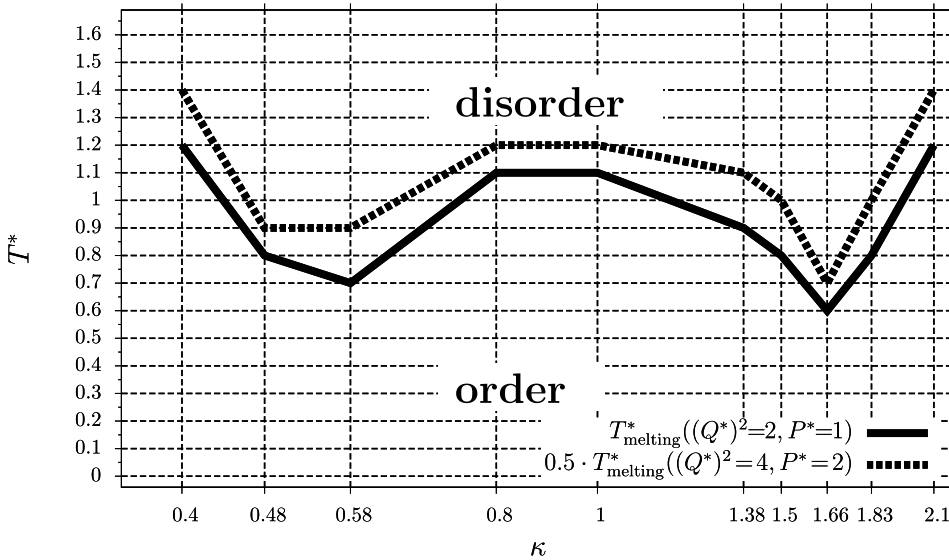


FIG. 18. Melting curve $T_{\text{melting}}^*((Q^*)^2=2, P^*=1, \kappa)$ that separates the ordered phase (at low temperatures) from the disordered phase (at high temperatures). In addition, a rescaled melting curve (using $\mu=2$) for $0.5 \cdot T_{\text{melting}}^*((Q^*)^2=4, P^*=2, \kappa)$ is shown, which has been obtained by applying the scaling laws specified in the text.

fraction η_{new} , the rescaling factor γ is related to the change in density according to

$$\gamma = \sqrt{\frac{\eta}{\eta_{\text{new}}}}. \quad (\text{C2})$$

As a consequence, the ground state cell volume is scaled with γ^2 .

Regarding the total potential energy, we assume that its scaling with respect to Q^2 and the rescaling of the positions follows the same law in the QHE system [see Eqs. (B2), (B1), and (7)], yielding

$$E_{\text{pot, new}}^{\text{GS}}(\gamma \mathbf{r}_{ij}, \hat{\mathbf{u}}_i, \hat{\mathbf{u}}_j; \mu Q^2) \approx \frac{\mu}{\gamma^5} E_{\text{pot}}^{\text{GS}}(\mathbf{r}_{ij}, \hat{\mathbf{u}}_i, \hat{\mathbf{u}}_j; Q^2). \quad (\text{C3})$$

Collecting all contributions, we obtain the following approximate expression for the enthalpy:

$$\begin{aligned} H_{\text{new}} &\approx \frac{\mu}{\gamma^5} E_{\text{pot}}^{\text{GS}}(Q^2) + \mu P \gamma^2 S_0^{\text{GS}} \\ &= \frac{\mu}{\gamma^5} H + \mu \left[\gamma^2 - \frac{1}{\gamma^5} \right] P S_0^{\text{GS}}. \end{aligned} \quad (\text{C4})$$

We check the applicability of this phenomenological scaling rule by calculating, as an example, enthalpies of a new system from the values of the enthalpies obtained at $(Q^*)^2 = 0.2$, $P^* = 0.1$ and $(Q^*)^2 = 20$, $P^* = 10$. The corresponding values for the enthalpy as functions of κ are presented in Figure 17. From these data, we can conclude that Eq. (C4) seems applicable for κ -values close to unity where the corresponding structures possess a 4-fold symmetry (T-configuration). For particles with larger aspect ratios, substantial deviations between the respective enthalpy curves occur.

2. Melting curve

As shown in Appendix B 2, the properties of the QHE system fulfill a parameter scaling relation also at finite temperature.

We now consider the question whether this rule can also be extended as an approximation to a system of soft particles. We are particularly interested in the melting curve, an example for which is shown in Figure 14 pertaining to the parameters $((Q^*)^2, P^*) = (2, 1)$. To test the scaling rule, we have

carried out the corresponding simulations for the case $\mu = 2$, i.e., $((Q^*)^2, P^*) = (4, 2)$ at temperatures $T^* = 0.2, 0.4, \dots, 3.2$. The rescaled melting curve for the new system, specified by the latter parameter set is displayed in Figure 18 in the rescaled form together with the original melting curve, corresponding to $((Q^*)^2, P^*) = (2, 1)$. We observe that the new, rescaled melting curve is similar in shape to the original one, but the two sets of data do not coincide: the rescaled curve lies over the entire κ -range above the reference curve; we attribute this fact to the stronger molecular overlaps leading to an increased binding strength. Specifically, we observe for all aspect ratios cohesion energies that are about three times higher for the parameter set $((Q^*)^2, P^*) = (4, 2)$ at the ground state; the factor three differs from the expected value of $\mu = 2$. In addition to the stronger overlaps, also the observed structural archetypes can differ between the two systems at the ground state. To be more specific, we obtained for $\kappa = 1.38$, a TH-configuration for $((Q^*)^2, P^*) = (4, 2)$, whereas for $((Q^*)^2, P^*) = (2, 1)$ a T-configuration is observed. We conclude that the scaling law put forward in Appendix B 2 only provides a rough estimate of the results obtained in actual calculations.

¹S. Blumstengel, S. Sadofev, and F. Henneberger, *New J. Phys.* **10**, 065010 (2008).

²S. Blumstengel, H. Glowatzki, S. Sadofev, N. Koch, S. Kowarik, J. P. Rabe, and F. Henneberger, *Phys. Chem. Chem. Phys.* **12**, 11642 (2010).

³C. Draxl, D. Nabok, and K. Hannewald, *Acc. Chem. Res.* **47**, 3225 (2014).

⁴R. Schlesinger, F. Bianchi, S. Blumstengel, C. Christodoulou, R. Ovsyanikov, B. Kobin, K. Moudgil, S. Barlow, S. Hecht, S. Marder, F. Henneberger, and N. Koch, *Nat. Commun.* **6**, 6754 (2015).

⁵N. Kleppmann and S. H. L. Klapp, *J. Chem. Phys.* **142**, 064701 (2015).

⁶H. Yanagi and S. Okamoto, *Appl. Phys. Lett.* **71**, 2563 (1997).

⁷V. M. Kaganer and E. B. Loginov, *Phys. Rev. Lett.* **71**, 2599 (1993).

⁸V. M. Kaganer, H. Mohwald, and P. Dutta, *Rev. Mod. Phys.* **71**, 779 (1999).

⁹J. Wang, R. M. Wolf, J. W. Caldwell, P. A. Kollman, and D. A. Case, *J. Comput. Chem.* **25**, 1157 (2004).

¹⁰M. Sinnokrot and E. Valeev, *J. Am. Chem. Soc.* **124**, 10887 (2002).

¹¹J. Petterson and T. Liljefors, *J. Comput. Chem.* **8**, 1139 (1987).

¹²S. L. Price and A. J. Stone, *J. Chem. Phys.* **86**, 2859 (1987).

¹³P. Golubkov and P. Ren, *J. Chem. Phys.* **125**, 064103 (2006).

¹⁴A. Chablo, D. Cruickshank, A. Hinchliffe, and R. Munn, *Chem. Phys. Lett.* **78**, 424 (1981).

¹⁵M. A. Bates and G. R. Luckhurst, *Liq. Cryst.* **24**, 229 (1998).

¹⁶T. Boublik, *Mol. Phys.* **69**, 497 (1990).

¹⁷C. Vega, *Mol. Phys.* **75**, 427 (1992).

- ¹⁸M. P. Neal and A. J. Parker, *Mol. Cryst. Liq. Cryst. Sci. Technol., Sect. A* **330**, 565 (1999).
- ¹⁹M. P. Neal and A. J. Parker, *Phys. Rev. E* **63**, 011706 (2000).
- ²⁰M. A. Miller, J. J. Shepherd, and D. J. Wales, *Mol. Phys.* **106**, 1655 (2008).
- ²¹G. Bautista-Carbajal and G. Odriozola, *J. Chem. Phys.* **140**, 204502 (2014).
- ²²J. Vieillard-Baron, *J. Chem. Phys.* **56**, 4729 (1972).
- ²³J. A. Cuesta, C. F. Tejero, and M. Baus, *Phys. Rev. A* **39**, 6498 (1989).
- ²⁴J. A. Cuesta and D. Frenkel, *Phys. Rev. A* **42**, 2126 (1990).
- ²⁵Y. Martínez-Ratón and E. Velasco, *Phys. Rev. E* **79**, 011711 (2009).
- ²⁶M. A. Bates and D. Frenkel, *J. Chem. Phys.* **112**, 10034 (2000).
- ²⁷V. M. Kaganer and M. A. Osipov, *J. Chem. Phys.* **109**, 2600 (1998).
- ²⁸B. J. Berne and P. Pechukas, *J. Chem. Phys.* **56**, 4213 (1972).
- ²⁹S. Sarman, *Phys. Chem. Chem. Phys.* **2**, 3831 (2000).
- ³⁰I. Mušević, M. Škarabot, U. Tkalec, M. Ravnik, and S. Žumer, *Science* **313**, 954 (2006).
- ³¹M. Škarabot, M. Ravnik, S. Žumer, U. Tkalec, I. Poberaj, D. Babič, N. Osterman, and I. Mušević, *Phys. Rev. E* **77**, 031705 (2008).
- ³²U. Ognysta, A. Nych, V. Nazarenko, M. Škarabot, and I. Mušević, *Langmuir* **25**, 12092 (2009).
- ³³M. Antlanger, "Ordered equilibrium structures in systems with long-range interactions," Ph.D. thesis, Technische Universität Wien, 2015, <http://katalog.ub.tuwien.ac.at/AC12656721>.
- ³⁴J. G. Gay and B. J. Berne, *J. Chem. Phys.* **74**, 3316 (1981).
- ³⁵C. Gray and K. Gubbins, *Theory of Molecular Fluids. Volume 1: Fundamentals*, International Series on Monographs on Chemistry Vol. 9 (Clarendon Press, Oxford University Press, New York, 1984).
- ³⁶D. Gottwald, G. Kahl, and C. N. Likos, *J. Chem. Phys.* **122**, 204503 (2005).
- ³⁷R. H. Byrd, P. Lu, J. Nocedal, and C. Zhu, *SIAM J. Sci. Comput.* **16**, 1190 (1995).
- ³⁸J. Fornleitner and G. Kahl, *Europhys. Lett.* **82**, 18001 (2008).
- ³⁹J. Fornleitner, F. Lo Verso, G. Kahl, and C. Likos, *Langmuir* **25**, 7836 (2009).
- ⁴⁰G. Doppelbauer, E. Bianchi, and G. Kahl, *J. Phys.: Condens. Matter* **22**, 104105 (2010).
- ⁴¹G. Doppelbauer, E. Noya, E. Bianchi, and G. Kahl, *Soft Matter* **8**, 7768 (2012).
- ⁴²E. Bianchi, G. Doppelbauer, L. Filion, M. Dijkstra, and G. Kahl, *J. Chem. Phys.* **136**, 214102 (2012).
- ⁴³E. Noya, I. Kolovos, G. Doppelbauer, G. Kahl, and E. Bianchi, *Soft Matter* **10**, 8464 (2014).
- ⁴⁴M. Antlanger, M. Mazars, L. Šamaj, G. Kahl, and E. Trizac, *Mol. Phys.* **112**, 1336 (2014).
- ⁴⁵M. Antlanger, M. Mazars, L. Šamaj, G. Kahl, and E. Trizac, "Rich polymorphic behavior of Wigner bilayers." *Phys. Rev. Lett.* (submitted).
- ⁴⁶H. J. C. Berendsen, J. P. M. Postma, W. F. van Gunsteren, A. R. H. J. DiNola, and J. R. Haak, *J. Chem. Phys.* **81**, 3684 (1984).
- ⁴⁷D. Fincham, *Mol. Simul.* **11**, 79 (1993).
- ⁴⁸K. J. Strandburg, *Rev. Mod. Phys.* **60**, 161 (1988).
- ⁴⁹W. Mickel, S. C. Kapfer, G. E. Schröder-Turk, and K. Mecke, *J. Chem. Phys.* **138**, 044501 (2013).
- ⁵⁰I. Georgiou, P. Ziherl, and G. Kahl, *EPL* **106**, 44004 (2014).
- ⁵¹B. Grünbaum and G. Shephard, *Tilings and Patterns* (W. H. Freeman and Company, 1987).
- ⁵²N. B. Vargaftik, B. N. Volkov, and L. D. Voljak, *J. Phys. Chem. Ref. Data* **12**, 817 (1983).
- ⁵³J. H. Miller, W. G. Mallard, and K. C. Smyth, *J. Phys. Chem.* **88**, 4963 (1984).
- ⁵⁴T. Heinemann, K. Palczynski, J. Dzubiella, and S. H. L. Klapp, *J. Chem. Phys.* **143**, 174110 (2015).
- ⁵⁵See <http://www.gromacs.org/Documentation/Manual> for Gromacs 4.5.4 Manual.
- ⁵⁶M. P. Allen and D. J. Tildesley, *Computer Simulation of Liquids*, Oxford Science Publications (Oxford University Press, 1989).
- ⁵⁷A. Giacometti, F. Lado, J. Largo, G. Pastore, and F. Sciortino, *J. Chem. Phys.* **132**, 174110 (2010).
- ⁵⁸T. Kirchhoff, H. Löwen, and R. Klein, *Phys. Rev. E* **53**, 5011 (1996).
- ⁵⁹K. Cui, O. Ivashenko, K. S. Mali, D. Wu, X. Feng, K. Mullen, S. De Feyter, and S. F. L. Mertens, *Chem. Commun.* **50**, 10376 (2014).
- ⁶⁰K. Cui, K. S. Mali, O. Ivashenko, D. Wu, X. Feng, M. Walter, K. Mullen, S. De Feyter, and S. F. L. Mertens, *Angew. Chem., Int. Ed.* **53**, 12951 (2014).
- ⁶¹A. Scheybal, T. Ramsvik, R. Bertschinger, M. Putero, F. Nolting, and T. Jung, *Chem. Phys. Lett.* **411**, 214 (2005).
- ⁶²G. Fang, Y. Shi, J. E. MacLennan, N. A. Clark, M. J. Farrow, and D. M. Walba, *Langmuir* **26**, 17482 (2010).
- ⁶³R. Koch, J. J. Finnerty, and T. Bruhn, *J. Phys. Org. Chem.* **21**, 954 (2008).
- ⁶⁴J. Roales, J. M. Pedrosa, P. Castillero, M. Cano, T. H. Richardson, A. Barranco, and A. R. González-Elipse, *ACS Appl. Mater. Interfaces* **4**, 5147 (2012).
- ⁶⁵H. Li, R. Zheng, and Q. Shi, *J. Phys. Chem. C* **116**, 11886 (2012).
- ⁶⁶G. Hlawacek and C. Teichert, *J. Phys.: Condens. Matter* **25**, 143202 (2013).
- ⁶⁷E. Zojer, N. Koch, P. Puschnig, F. Meghdadi, A. Niko, R. Resel, C. Ambrosch-Draxl, M. Knupfer, J. Fink, J. L. Brédas, and G. Leising, *Phys. Rev. B* **61**, 16538 (2000).
- ⁶⁸C. Simbrunner, *Semicond. Sci. Technol.* **28**, 053001 (2013).
- ⁶⁹T. Heinemann, K. Palczynski, J. Dzubiella, and S. H. L. Klapp, *J. Chem. Phys.* **141**, 214110 (2014).
- ⁷⁰E. Bianchi, G. Kahl, and C. Likos, *Soft Matter* **7**, 8313 (2011).
- ⁷¹E. Bianchi, C. N. Likos, and G. Kahl, *ACS Nano* **7**, 4657 (2013).
- ⁷²E. Bianchi, C. Likos, and G. Kahl, *Nano Lett.* **14**, 3412 (2014).
- ⁷³P. D. J. van Oostrum, M. Hejazifar, C. Niedermayer, and E. Reimhult, *J. Phys.: Condens. Matter* **27**, 234105 (2015).